

Sensifi: A Wireless Sensing System for Ultra-High-Rate Applications

Chia-Chi Li, Vikram K. Ramanna, Daniel Webber, Cole Hunter, Tyler Hack, and Behnam Dezfouli*

Internet of Things Research Lab, Santa Clara University, USA

{cli1, vramanna, dwebber, chunter, thack, bdezfouli}@scu.edu

Abstract—Wireless Sensor Networks (WSNs) are being used in various applications such as structural health monitoring and industrial control. Since energy efficiency is one of the major design factors, the existing WSNs primarily rely on low-power, low-rate wireless technologies such as 802.15.4 and Bluetooth. In this paper, we strive to tackle the challenges of developing *ultra-high-rate* WSNs based on 802.11 (WiFi) standard by proposing Sensifi. As an illustrative application of this system, we consider vibration test monitoring of spacecraft and identify system design requirements and challenges. Our main contributions are as follows. First, we propose packet encoding methods to reduce the overhead of assigning accurate timestamps to samples. Second, we propose energy efficiency methods to enhance the system’s lifetime. Third, we reduce the overhead of processing outgoing packets through network stack to enhance sampling rate and mitigate sampling rate instability. Fourth, we study and reduce the delay of processing incoming packets through network stack to enhance the accuracy of time synchronization among nodes. Fifth, we propose a low-power node design for ultra-high-rate applications. Sixth, we use our node design to empirically evaluate the system.

Index Terms—Sensing, 802.11, WiFi, Low-Power, RTOS, Packet Processing, Vibration Test.

I. INTRODUCTION

The objective of a Structural Health Monitoring (SHM) system is to provide an automated and real-time assessment of a structure’s ability to serve its intended purpose [1], [2]. SHM systems have been adopted in various applications such as aerospace, civil, and mechanical monitoring [3]–[5]. In these systems, sensors are deployed on a structure to assess its structural and mechanical health. SHM usually involves a labor-intensive process to attach sensors and route power and signal transmission wires through the structure without damaging it.

The significant reductions in the cost and energy consumption of microprocessors, wireless transceivers, and sensors have facilitated the development of Wireless Sensor Networks (WSNs) for SHM as well as applications such as Process Automation (PA), Factory Automation (FA), and medical monitoring [6]. WSNs are being used in SHM applications to monitor spacecraft, aerial vehicles, high-rise buildings, dams, highways, and bridges [3], [7]–[9]. In these applications, sensor nodes collect information such as acceleration,

ambient vibration, load, and stress at sampling frequencies usually above 100 Hz [10]. The replacement of cables with wireless links reduces design, deployment, and maintenance costs. Also, wireless links offer higher reliability compared to cables that are subject to wear and tear.

A prominent example of SHM is spacecraft vibration monitoring. Successful launching of a spacecraft is a complicated procedure that can take years to plan and hundreds of millions of dollars to fund. As a result, it is essential to perform extensive tests on a spacecraft before its launch to ensure success and durability. While there are numerous ways a spacecraft can fail during a launch, we focus on vibrational analysis and testing due to the unique challenges imposed. These tests are performed to analyze a spacecraft’s mechanical durability against the launch’s powerful vibrational forces. Companies simulate these experiments by conducting nondestructive vibrational experiments on their spacecraft to ensure they can survive the high g-forces required to leave the atmosphere [11]. During these tests, the spacecraft is placed on a shaker table and mounted with sensors connected, via *cables*, to the Data Acquisition (DAQ) modules in the control room. These tests are conducted with a large number of wired accelerometers (more than 200), simultaneously sampled by expensive, high-performance DAQ modules [12]. The large number of nodes and the high sampling rate (around 50 kHz) result in generating a massive amount of data that must be collected from the structure. This results in a disarray of wired connections that make installing and debugging these sensors an excessively laborious and time-consuming process. In addition to the setup difficulties, the extra weight applied to the spacecraft by the cables can skew vibrational measurement results [13]. The cables also introduce electrostatic noise that affect data collection accuracy.

In this paper, we use the term *ultra-high-rate* to refer to the systems whose data transmission rate is in the range of few hundreds of Mbps to a few Gbps. In addition to the spacecraft monitoring applications mentioned above, applications such as FA, Power Systems Automation (PSA), and Power Electronics Control (PEC) are representative of ultra-high-rate scenarios [14]. In general, a set of requirements must be considered when designing a WSN for these applications. Besides satisfying the high sampling rate required by these applications, the additional requirements are: (i) *liveness*:

*Corresponding Author.

collecting data from all the nodes while sampling is in progress, (ii) *scalability*: live data collection from a large number of nodes (e.g., more than 200 in spacecraft monitoring), (iii) *energy efficiency*: the nodes' longevity must satisfy the duration requirement of the experiment, (iv) *accuracy*: accurate timestamps must be assigned to the samples, and (v) *reliability*: lossless collection of raw samples is required. We detail these requirements as follows.

Due to the sensor nodes' resource limitation, energy efficiency has been considered as the main factor when designing WSNs. As a result, 802.15.4 and 802.15.1 are the primary wireless technologies used in existing works [15]. However, these standards cannot be used for the live transmission of samples collected at a high rate [14]. For example, a node collecting 12-bit samples at 50 kbps needs to communicate at 600 kbps, excluding the overhead of the samples' timestamps. In this case, the 250 kbps data rate provided by the 802.15.4 standard is less than the communication demand of *one node*. Therefore, the wireless technologies used in current industrial networks, such as WirelessHART [16], WIA-PA [17], ISA 100 [18], WSA-FA/IO-Link [19], and WISA [20] cannot be used for ultra-high-rate sensing applications.

A naive approach for enhancing sampling rate is to postpone data transmission by storing the samples in RAM or a memory card, and then transfer the data once the experiment is complete or whenever the user requests for data delivery [21]–[24]. This method, however, does not satisfy the liveness requirement. For example, spacecraft vibration tests require live response monitoring and making adjustments to the test configuration parameters. Also, this approach prevents the test engineer from identifying malfunctioning nodes until after the test. Besides, frequent placement and removal of nodes in hard-to-access areas are not desirable.

Compression and in-network processing methods have been proposed to reduce the amount of data sent per node. One common approach for time-series-based data is to compute auto-regressive/auto-regressive moving average (AR/ARMA) coefficients locally by each node and transmit this data instead of the raw sensor data [25], [26], or use AR methods with random decrements to compress sensor data by averaging a large number of time segments [27]. Another approach is to process data locally and send samples only if a particular event is detected [28], [29]. Nevertheless, these approaches are lossy and cannot be used in scenarios where raw data collection is required to implement various data analysis methods [8], [29]. Furthermore, even if a drop in monitoring accuracy is tolerated, the compression level provided by these methods is not enough to adapt low-rate wireless technologies for ultra-high-rate applications. Finally, given the high processing overhead of compression algorithms, implementing them on sensor nodes results in interruptions in the sampling process.

Variations of inter-sample delay make assigning accurate timestamps to samples more challenging, and achieving

sampling rate stability is particularly difficult in ultra-high-rate applications. Running additional tasks on the processor causes interruptions in the sampling process and variations of the sampling rate. Therefore, the effect of running additional tasks, such as packet processing and wireless transmission, must be minimized. The existing works have identified this challenge; however, they do not offer a comprehensive evaluation or mitigation to the problem [22], [30]. In addition to the effect of sampling stability on timestamp assignment, achieving accurate time synchronization in 802.11 networks is particularly challenging. The existing time synchronization methods proposed for WSNs primarily handle the uncertainties introduced by the 802.15.4 stack [23]. However, these uncertainties are harder to capture and mitigate when using complicated wireless standards such as 802.11. Without accurate time synchronization and timestamping, damage detection and localization become impossible due to mode shape errors [23], [31], [31]–[33].

In this paper, we propose Sensifi, a system based on 802.11 (WiFi) standard for ultra-high-rate sensing applications. Towards tackling the underlying challenges of developing this system, *the main contributions of this paper are as follows*: *First* (§IV), we show that assigning accurate timestamps (sub- μ s accuracy) to samples introduces a significant overhead and wastes precious payload bytes and wireless communication bandwidth. We propose three encoding methods, based on the distribution of inter-sampling intervals, to reduce payload overhead. These methods achieve various levels of payload efficiency and execution time. By reducing the amount of data sent per node, we enhance system scalability and reduce the nodes' energy consumption to transmit the collected samples. *Second* (§V), we propose methods that can reduce the energy consumption of nodes during their inactivity periods. In particular, since the 802.11 transceiver is the primary energy consumption source, we study two energy-efficiency methods: periodic association with the Access Point (AP), and extended-period beacon reception. In the former method, each node periodically associates with the AP and checks for control packets. For the latter method, we increase the listen interval of nodes to enhance their beacon reception energy efficiency. We also propose and empirically evaluate mechanisms to enhance the energy efficiency of these methods further. Depending on the application scenario, the proposed methods and configurations can be used to achieve the desired energy efficiency level. *Third* (§VI), we show that preparing and processing outgoing packets by the network stacks introduce a non-negligible delay that must be minimized to increase sampling rate and enhance its stability. Our work reveals that bypassing transport layer processing is essential to minimize the effect of packet processing on sampling rate, which also translates into the higher performance of timestamp encoding. *Fourth* (§VII), we present a thorough study of time synchronization and identify the challenges caused by network stack complex-

ity. Through empirical evaluation of time synchronization error, we observed that placing the time synchronization functionality in the driver or the layers above it cannot achieve sub- μs accuracy. To address this challenge, we move the time synchronization function to the 802.11 subsystem, between the packet decoding logic and driver, and confirm that the maximum error is bounded by $0.25 \mu\text{s}$. *Fifth* (§VIII), we present a modular and low-power node design, which incorporates a high-rate Analog to Digital Converter (ADC), a high-accuracy sensor, an efficient power distribution unit, and components that facilitate system development. *Sixth* (§IX), using our node design, we empirically evaluate various aspects of the system and demonstrate the performance enhancements achieved with the proposed methods.

The wireless technology used in this work is 802.11ac (WiFi 5), and the primary goal is to develop a solution for the vibration test of spacecraft (§II). Nonetheless, the methods proposed in this paper can be employed for developing WSN systems for applications such as PA, FA, Building Automation System (BAS), intra-vehicle communication, and Wireless Avionics Intra-Communications (WAIC). This work is based on two assumptions: First, wireless communication happens over one hop, between the nodes and AP. Second, although the system supports live data collection from the nodes, we do not impose any deadline on packet delivery delay [34]. Specifically, we do not propose any channel access arbitration mechanism for real-time packet delivery. Nevertheless, by proposing methods that reduce the amount of data generated per node, we enhance network scalability regardless of the underlying channel access method.

Compared with the existing works that rely on TinyOS [8], [30], [35], Linux [36], [37], or theoretical performance analysis [28], [38], we use the two widely-used Real-Time Operating Systems (RTOSs) targeting resource-constrained devices: FreeRTOS [39], [40] and ThreadX [41], [42]. Also, we use the network stacks available for these RTOSs, namely, LwIP [43], NetX [44], and NetXDuo [45]. Therefore, *a unique aspect of our work is identifying and tackling the underlying challenges of using these tools for developing ultra-high-rate applications.*

The rest of this paper is organized as follows. Section II reviews the spacecraft monitoring application. Section III overviews system architecture. Sampling and packet encoding methods are presented in Section IV. Duty cycling methods for reducing the energy consumption of the system are presented in Section V. We propose methods to reduce the latency of packet processing in Section VI. Challenges and solutions for achieving high-accuracy time synchronization are studied in Section VII. Section VIII details hardware design. Section IX presents overall system evaluation results. We summarize related work in Section X. We conclude the paper in Section XI.

II. SAMPLE APPLICATION SCENARIO

Although the system proposed in this paper can be used in a variety of ultra-high-rate sensing applications, we focus on spacecraft monitoring to identify and clarify the unique challenges of this application and frame our system design.

Space and aerospace companies send satellites and other spacecraft into space for various purposes such as research, communication, and video broadcasting. The launch environment is characterized as a random, non-stationary, and short transient duration. Spacecraft vibration test monitoring is a SHM application that requires live, ultra-high-rate data collection from a large number of nodes (usually more than 200) [46], [47]. The main objective of this test is to excite components, subsystems, and nonstructural hardware that respond to the launch environments. There are three main types of vibration tests that are run on spacecraft: random vibration, sinusoidal vibration, and shock [12]. *Random vibration* targets two cases: (i) where the normal random vibration measurement range frequency is less than 250 Hz, and (ii) high resonance spikes, which can be up to 10 kHz during the acoustic test. In random vibration test, the spacecraft is subjected to quasi-random vibrations within some specific limits. The magnitude of these resonance spikes depends on the target object's mass and the load attached to the target object. To effectively discover spacecraft design flaws, some system-level random vibration tests are combined with the acoustic test range to cover the above two cases [47]. For example, Jet Propulsion Laboratory (JPL) recommends random vibration test to be combined with the acoustic test in the frequency range of 10 Hz to 10 kHz [47], and NASA General Vibration Laboratory (GVL) recommends the vibration test frequency to reach 3 kHz [11]. *Sinusoidal vibration* is when the spacecraft is accelerating at a constant frequency with varying amplitudes. To minimize the dynamic response or amplification of the acceleration, the frequency of interest is selected to be significantly lower than the fundamental vibration frequency. Test designers sweep frequency range from 5 Hz to 60 Hz to identify natural resonances of the spacecraft [48]. For example, NASA Goddard Space Flight Center (GSFC) uses a sine sweep vibration input with the range from 5 Hz to 60 Hz [48]. *Shock testing* is when the spacecraft is subject to high impulse vibrations. These are typically required to simulate pyrotechnics explosion for separating the stages of the spacecraft. Typical spacecraft shock tests have low frequency range, from hundreds to thousands of Hz [49] with acceleration range up to 300 g-force [50]. JPL pyroshock test is characterized by its high peak acceleration from 300 g-force to 300 kg-force and high frequency range from 100 Hz to 1 MHz [51]. In this paper, we primarily focus on developing a system for random vibration and sinusoidal tests, because the sensor and ADC used in our node design cannot cover the measurement range required by shock testing. Nevertheless, the proposed methods facilitate the development of a shock testing system.

The setup for both the sinusoidal and random vibration tests are alike. The spacecraft is attached to a large shake table, and then, accelerometers are mounted. This is referred to as the *mounting phase* or *Idle Phase* because nodes do not perform sampling during this phase. This phase is the most laborious and time-consuming step of the process. Each sensor has a short wire with a connector attached at the end. The engineers at Space Systems Loral (SSL) have informed us that depending on sensor placements, partial disassembly of the satellite may occur to facilitate the sensor's placement in the exact locations needed to collect data. From there, longer cables are run from the sensors to the DAQ. The mounting process can take between one to two weeks to attach the devices before the test is started. The cables have to be carefully mounted to the spacecraft for two primary reasons: avoid damage to the spacecraft during the test, and prevent significant changes to the spacecraft's load properties. The latter is critical because if one wants to add more sensors to study the system better, the added weight may alter the system's load properties, which is in direct opposition to the test's goal. This is because the more sensors added, the more likely the results are not representative of the realistic properties of the spacecraft [13]. Given that each cable performs slightly differently and has a unique transfer function, an individual profile needs to be generated so that these differences can be calibrated out. This wired solution is costly and lacks versatility.

After the mounting phase, each sensor has to be manually verified. Verification is critical because engineers need to ensure that all sensors are functioning properly before the test is conducted. After verification, the tests begin. This is referred to as the *Sampling Phase*. During the test, sensors are sampled continuously for 20 to 40 minutes.

When developing a WSN for this application, during the mounting phase, nodes must operate in an energy-efficient manner to ensure enough energy is left for the Sampling Phase. Live transmission of sampled data is essential to allow the system engineers to detect faulty nodes and adjust test parameters dynamically. Supporting network scalability is critical to allow concurrent, live data collection from more than 200 nodes. During the Sampling Phase, the sampling rate of nodes must satisfy the system requirement. Also, accurate assignment of timestamps to samples is necessary.

III. SYSTEM OVERVIEW

The system's three primary components are nodes, AP, and a server. Each node is a wireless sensor device capable of sampling, processing, and wireless communication. AP receives packets from nodes and forwards them to the server. More than one AP may be required to address system's scalability requirement. The server coordinates network operation, decodes the received packets, processes the collected data, and generates time synchronization packets.

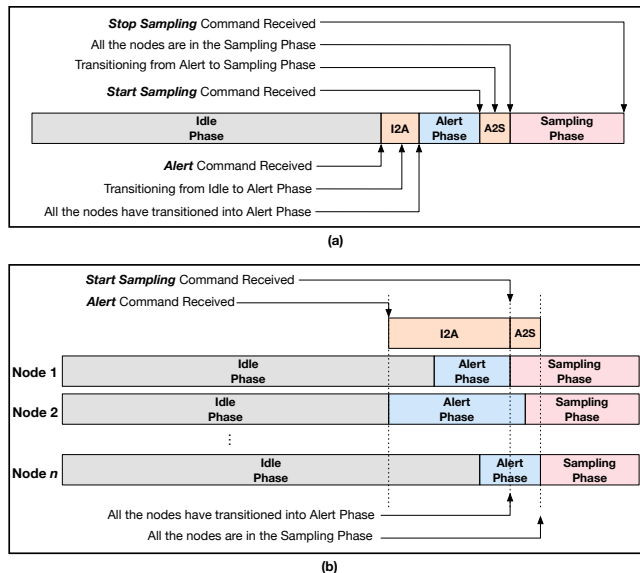


Fig. 1. (a) The operational phases of the overall system. (b) The operational phases of nodes. Since the transition time of nodes varies depending on energy efficiency configuration, transition periods exist from the overall system's point of view. These transition periods are named Idle to Alert (I2A) and Alert to Sampling (A2S).

The basic components of a node are sensor (an accelerometer in our node design), ADC, processor, and wireless transceiver. The ADC used in our node design is capable of sampling at up to 500 ksps and is interfaced with the processor using Serial Peripheral Interface (SPI) bus. Sample collection and encoding are explained in §IV. The wireless transceiver used in this paper is based on the 802.11 standard to support the live transmission of collected samples. Specifically, the System on a Chip (SoC) used in our node design is based on CYW54907 [52], which supports 802.11ac. All the results collected in this paper use the 802.11ac standard. This SoCs includes two ARM-Cortex R4 processors, where one processor is dedicated to the *application subsystem*, and the other one is assigned to the *wireless subsystem*. The former subsystem runs user code, and the latter subsystem runs 802.11 firmware to handle time-critical tasks such as backoff and acknowledgment packet generation. We discuss hardware design in §VIII.

Figure 1 shows the operational phases of the WSN. Referring to the spacecraft monitoring application (§II), we detail the operational phases of Figure 1(a) as follows. During the mounting phase, which may take between one to two weeks, nodes are mounted on the spacecraft. Before mounting each node, the node is turned on and enters the Idle Phase. During this phase, the power consumption of the nodes must be minimal. We refer to the nodes' power status in Idle Phase as *deep sleep*, which is required to achieve maximum energy efficiency. Once a node receives the *Alert Command* from the server, the node transitions into Alert Phase and waits to

receive a *Start Sampling* command from the server to start the *Sampling Phase*. Figure 1(b) shows this transition for three nodes. Since the nodes transition from Idle Phase to Alert Phase at different times, there is a transition period for the system to ensure all the nodes are in Alert Phase. This delay is referred to as the Idle to Alert (I2A) transition.

We refer to the power status of the nodes in Alert Phase as *sleep*. Compared to the Idle Phase, Alert Phase provides a higher level of responsiveness to commands. Specifically, depending on the energy efficiency mode employed, the time it takes for nodes in the Idle Phase to receive the alert command varies between a few seconds to a few minutes; whereas, in alert mode, the delay between sending the Start Sampling command and starting the Sampling Phase is up to a few seconds. This delay is referred to as the Alert to Sampling (A2S) transition. The duration of I2A and A2S depend on the energy efficiency methods used (§V). During the Sampling Phase, each node collects and sends sensory data to the AP.

The different energy efficiency methods used during the Idle Phase and Alert Phase justify the need for a low-cost transition from Idle Phase to Sampling Phase. Specifically, if we send a Start Sampling command to the nodes in Idle Phase, they start sampling at time instances that may be up to a few minutes apart. Therefore, while some nodes are consuming higher energy to collect and transmit samples, the rest are still in low-power mode; and this results in partial system monitoring and energy waste by some nodes. Considering the high energy consumption of nodes during the Sampling Phase, we need to ensure all the nodes start the Sampling Phase almost synchronously, and this is not possible considering the deep sleep mode used during the Idle Phase. Therefore, we use an intermediate energy efficiency method, i.e., the Alert Phase, to minimize the intervals between the instances the nodes transition into Sampling Phase.

Although spacecraft monitoring is featured in this paper, the methods proposed in the subsequent sections can be used to tailor the system for various types of applications. For example, for an application that requires periodical sampling of a structure at long intervals, the above three phases can be used, as Figure 2(a) shows. For applications where the interval between Sampling Phases is short, only the Alert Phase can be used to enhance the energy efficiency of the system, as Figure 2(b) shows.

Algorithm 1 presents the operation of a node during the Sampling Phase. During this phase, each node performs three types of tasks sequentially: sampling, encoding, and packet transmission. These operations are repeated as long as the Stop Sampling command is not received from the server. The sampling task collects s samples and their timestamps (lines 4 to 9). We refer to s as the *sampling batch size*. The collected samples and timestamps are then encoded to reduce the overhead of timestamp assignment (lines 10 to 12), as we

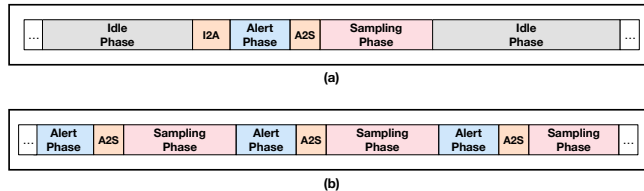


Fig. 2. (a) A system with long intervals between Sampling Phases. (b) A system with short intervals between Sampling Phases.

Algorithm 1: Overall Control Flow of Each Node During the Sampling Phase

```

1 function main_thread()
2   n = 0 /* initialize packet sequence number */
3   while sampling_phase do
4     n = n + 1
5     for i = 0; i < s; i++ do
6       /* s is the maximum number of samples per
7        packet. We refer to s as sampling
8        batch size */
9       S[i] = get_ADC_sample() /* 2 bytes */
10      T[i] = get_nanosec_clock()
11      if i > 0 then
12        I[i] = T[i] - T[i - 1] /* calculate
13         inter-sample interval */
14      intv_freq_count(I[s], H[s], used) /* calculate
15      repetitions per inter-sample interval */
16      intv_freq_ranking(H[s], used) /* rank
17      inter-sample intervals based on
18      repetitions */
19      packet_encoding(H[s], count, S[s], I[s], pkt)
20      packet_preparation(pkt)
21      packet_send(pkt)
22   return

```

discuss in §IV. Once packet encoding is complete, the proper data structures are allocated to the packet (line 13), and then the packet is processed by the communication protocol stack (line 14). We discuss packet creation and processing in §VI.

IV. SAMPLING AND PACKET ENCODING

The server collecting sampling data must be able to accurately reconstruct the signals measured by the nodes. Considering the application scenario discussed in §II, reconstructing temporal vibration information from the nodes' collected samples is crucial to conducting accurate vibration test monitoring. If samples are collected at exact equidistant intervals, we can include a single timestamp per packet to specify the timestamps of all the samples included in the packet. However, there are variations in sampling intervals; thus, using a single timestamp per packet reduces the timing accuracy of the measurement event [53]. On the other hand, assigning a per-sample timestamp introduces a significant overhead.

In this section, we propose methods for efficient and lossless compression of timestamps, considering packet size limitation in the 802.11 standard. In addition to *compression efficiency*, we also consider *execution time* as an important design metric to minimize the effect of encoding on sampling rate. We study the variability of sampling intervals using our node design, which collects samples at rates up to 500 ksp/s, and propose three timestamp encoding methods based on the statistical distribution of sampling intervals. By reducing the overhead of wireless communication, the proposed methods enhance energy efficiency, scalability, and reliability.

A. Sampling Interval Variations

In an ideal situation, when an ADC continuously collects samples, the intervals between samples are fixed. However, most ADCs include a built-in sample-and-hold function, making the ADC unable to make an instantaneous conversion [54]. For example, the modern Successive Approximation Register (SAR) ADC design has an internal switched-capacitor Digital to Analog Converter (DAC), also known as charge redistribution DAC. The DAC uses capacitors to store the voltage at the input and uses a switch to disconnect the capacitors from the input [55]. The switched-capacitor structure's conversion time scales exponentially with the resolution of ADC. Besides resolution, the amount of time to hold the capacitor value, impedance of the internal analog multiplexer, output impedance of the analog source, and the switch impedance are factors impacting ADC's conversion time. In addition to the internal operation of ADC, the processor can also affect sampling intervals. For example, sampling intervals are affected by variations in the communication bus clock with the ADC, switching between tasks, and packet processing.

We placed the nodes inside a controlled temperature chamber and used a high-accuracy logic analyzer to capture inter-sample intervals. *For these experiments, the only task being run by the nodes is sampling.* Figure 3 shows inter-sample intervals. For 100 ksp/s, we observe up to $0.11 \mu\text{s}$ variations around the mean value of $10 \mu\text{s}$, and for 500 ksp/s, the variations are up to $0.016 \mu\text{s}$ around the mean value of $2 \mu\text{s}$. Considering the 25 ns timing precision provided by the logic analyzer, nearly 99% of the intervals are within four to six classes for both sampling rates, and the other 1% of the intervals are distributed among several classes. Each class in the 1% distribution contributes to less than 0.2% of the total samples. Also, as it can be observed, the ambient temperature has a negligible effect on the number of classes because the temperature coefficient of switched capacitors is less than 1 ppm/ $^{\circ}\text{C}$ [56].

Based on these observations, considering inter-sample variations is a key factor to improve timestamp encoding efficiency. *If we include only one timestamp per packet, then these errors accumulate as more samples are included in the packet.* For example, when sampling at 500 ksp/s, for a

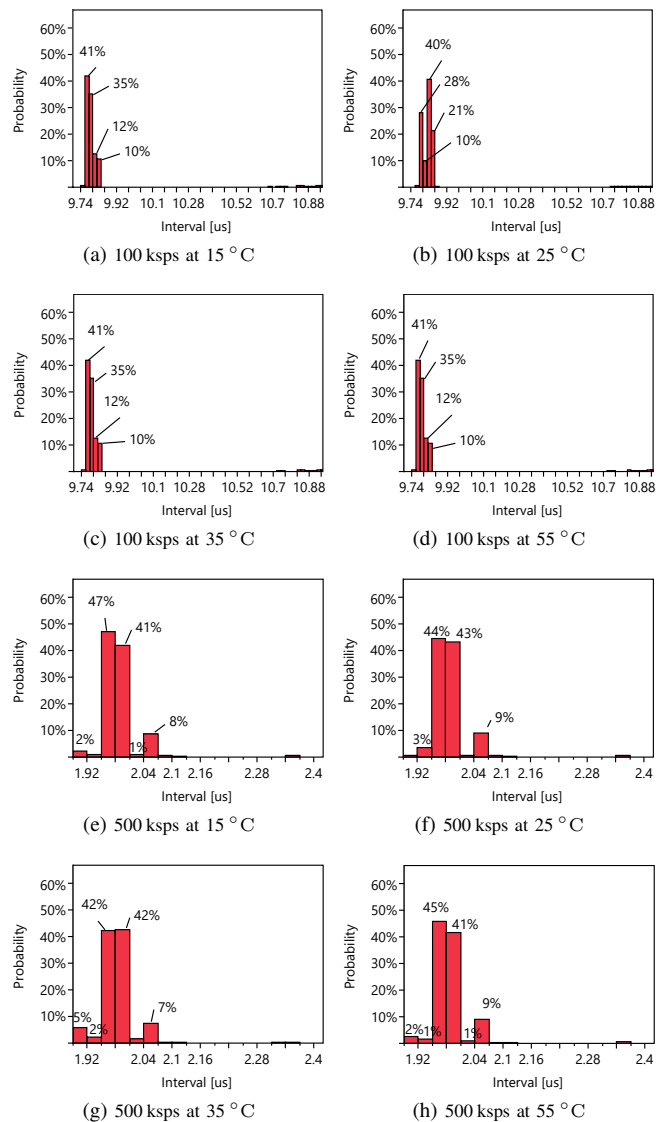


Fig. 3. Distribution of sampling interval under different ambient temperature conditions. (a)-(d): Sampling rate 100 ksp/s. (e)-(h): Sampling rate 500 ksp/s. For these experiments, the only task being run by the nodes is sampling. Nearly 99% of the intervals are within four to six classes, and the remaining 1% of the intervals are distributed among several classes.

packet including 500 samples, the error of the timestamp inferred for the last packet is about $8 \mu\text{s}$. This error is about $55 \mu\text{s}$ for 100 ksp/s. For the server to reconstruct the accurate temporal vibration information from these samples, a timestamp for each collected sample is required. In the following, we propose methods to address this requirement.

B. Encoding Methods

1) *Baseline*: Our baseline method refers to assigning a timestamp per sample without applying any encoding. We discuss two baseline methods as follows.

Overhead		Data
2 [B]	$s \times 8$ [B]	$s \times 2$ [B]
Seq#	Timestamp Table (TST)	s Samples

(a): Packet Format with 8 bytes Timestamp (Baseline-8B)

Overhead		Data
2 [B]	$s \times 6$ [B]	$s \times 2$ [B]
Seq#	Timestamp Table (TST)	s Samples

(b): Packet Format with 6 bytes Timestamp (Baseline-6B)

Overhead							Data
2 [B]	1 [B]	8 [B]	1 [B]	1 [B]	$(c \times k) / 8$ [B]	$((s-1) \times \log_2 c) / 8$ [B]	$s \times 2$ [B]
Seq#	Type	Base Time	c	k	Timestamp Table (TST)	Timestamp Indexing Table (TIT)	s Samples

(c): Packet Format with Interval Encoding (IENC)

Overhead								Data
2 [B]	1 [B]	8 [B]	2 [B]	12 [B]	2 [B]	$(2 \times o)$ [B]	$(s \times 3) / 8$ [B]	$s \times 2$ [B]
Seq#	Type	Base Time	C_1	$C_2 \dots C_7$	TST Size	Timestamp Table (TST)	Timestamp Indexing Table (TIT)	s Samples

(d): Packet Format with Interval Outlier Encoding (OENC)

Overhead								Data
2 [B]	1 [B]	8 [B]	2 [B]	6 [B]	2 [B]	o [B]	$(s \times 3) / 8$ [B]	$s \times 2$ [B]
Seq#	Type	Base Time	C_1	$C_2 \dots C_7$	TST Size	Timestamp Table (TST)	Timestamp Indexing Table (TIT)	s Samples

(e): Packet Format with Differential Outlier Encoding (D-OENC)

Fig. 4. Packet formats of various timestamp encoding methods. (a) Packet format with an 8 byte timestamp per sample (Baseline-8B). (b) Packet format with an 6 byte timestamp per sample (Baseline-6B). (c) Packet format using Interval Encoding (IENC). (d) Packet format using Outlier Encoding (OENC) where 2 bytes are assigned to each outlier. (e) Packet format with Differential Outlier Encoding (D-OENC) where 1 byte is assigned to each outlier.

The SoC used in our design provides a nanosecond timer that can be read into an 8-byte variable. Figure 4(a) shows the baseline packet format where an 8-byte timestamp is added per sample. Each sample is 2 bytes. *Seq#* is the packet sequence number. Considering the 1472 byte Maximum Transmission Unit (MTU), we can include a maximum of 147 samples per packet, which means 80% of the payload is occupied by timestamps. We refer to this method as *Baseline-8B*, as demonstrated in Figure 4(a).

The time duration provided by an 8 byte, nanosecond-granularity variable is over 500 years, which is more than what is required in real-world applications. Assuming time synchronization is only required during the Sampling Phase, a 60-minutes Sampling Phase requires 42 bits to provide nanosecond timing accuracy. Considering the time needed for Sampling Phase, a 6-byte nanosecond timestamp, which wraps around every 78 hours, fulfills our need. With a 6-byte timestamp, we can include a maximum of 183 samples per packet, introducing a 75% overhead per packet for timestamp information. We refer to this method as *Baseline-6B*, as demonstrated in Figure 4(b).

To reduce the overhead of adding timestamps and increase the number of samples sent per packet, we present three lossless encoding methods and compare their performance

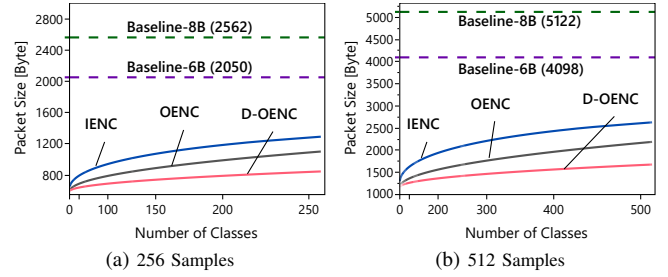


Fig. 5. Packet size comparison across the three encoding methods. X-axis represents the number of classes in a batch of samples (s). Note that the x-axis increments by the power of 2.

against the baselines, as follows.

2) *Interval Encoding (IENC)*: The basic idea of this encoding method is to encode sampling interval classes into an index table. The overhead of timestamp encoding varies based on the distribution of the interval classes. Figure 4(c) shows the packet format of this encoding method. The two main tables used for timestamp encoding are Time-stamp Table (TST) and Time-stamp Indexing Table (TIT). The TST includes the classes of sample conversion intervals, which takes a maximum of 2 bytes to encode each interval (instead of 8 bytes). The total number of interval classes is denoted by the variable c . The number of bits required to represent each class is k , denoting the interval as a coefficient of 1 ns. Two variables c and k are added to the packet before the TST to inform the server about the size of the table to decode. For each sample $S[i]$ where $i > 1$, there is a corresponding entry in the TIT that refers to an entry of TST. Since TST has c entries, each entry in the TIT is $\log_2 c$ bits. With this, the TIT specifies the interval between each pair of consecutive samples. *Base Time* is the nanosecond timestamp of the first sample in the packet. By using Base Time, TST, and TIT, we can reconstruct the temporal sample information in the server.

Figure 5 shows theoretical comparison of packet size using different encoding methods. The x-axis of sub-figures (a) and (b) represent the number of possible interval classes considering 256- and 512-sample batches, respectively. Comparing with the baseline methods (horizontal lines), IENC reduces payload overhead by at least 48% compared to Baseline-8B and 35.6% compared to Baseline-6B.

With 512-sample batches, IENC hits the payload constraint when more than 12.5% of the intervals are unique. Once payload limitation is reached, IENC stops processing the TST and encodes the samples as two 256-sample packets. Notice that these two sub-divided packets have their own Base Time, TIT, and TST to ensure a packet loss would not influence the other one. We use the *Type* field to notify the server whether this packet was sub-divided. The value 0 means only one packet, value 1 means the first of two packets, and value 2 represents the second of two packets. It is worth noting

that, as Figure 5(a) shows, when 256-sample batches are collected, IENC’s worst case scenario consumes 1292 bytes, which is within the payload limitation. Therefore, there is no possibility that a third packet is needed when the sampling size is 256.

A drawback of IENC is that the TIT field occupies about 25% of the payload in the worst case. To further improve encoding efficiency, we note that IENC does not consider the repetitions of interval classes. We rely on this observation and propose two other encoding methods, as follows.

3) *Outlier Encoding (OENC)*: This method leverages the statistical pattern of the classes to reduce encoding overhead. Figure 3 shows that a few classes include the majority of the outlier intervals. We refer to these classes as $C1$ through $C7$. For example, in 512-sample batches, only 6 intervals are outside of these major classes, in most cases. We use this observation to further reduce the TIT size. Figure 4(d) shows the packet format used by OENC. The basic idea is to reduce TIT size by using a 3-bit index for each sample. This method uses a fixed TIT size instead of letting the size grow by the number of interval classes. In the TIT, there is a 3 bit index for each sample; therefore the size of TIT is $s \times 3$ bits. Index values 000, 001, and 010 are referred to as $C1$, $C2$, or $C3$, respectively. If the index of a sample is 111, it means the interval is an outlier and must be found in the TST. For each index value 111 in the TIT, there is a corresponding outlier value in the TST. In other words, the number of entries with index value 111 in the TIT is the same as the number of entries in TST. The *TST Size* field is used to inform the server about the size of TST.

Figure 5 shows that OENC reduces packet payload size by at least 56% compared to *Baseline-8B* and 45% compared to *Baseline-6B*. Compared to IENC, the reduction is about 8% with the maximum number of outliers. However, OENC hits the payload constrain when more than 23% of the intervals in a 512-sample batch are unique. Once it reaches the limit, OENC stops processing the TST and sub-divides the samples into two packets. These two packets create their own $C1$ to $C7$, TST, TST size, and the TIT field values. Figure 5(a) shows that OENC’s worst case scenario with 256 samples consumes 1132 bytes, which is within the payload limit. As Figure 4(d) shows, TIT always consumes 96 and 192 bytes of the payload for 256- and 512-sample batches, respectively; whereas, TST grows as the variations of sampling intervals increase. In the worst case, OENC’s TST field occupies about 46% of the payload, which is the second-largest payload consumption field after the samples field.

4) *Differential Outlier Encoding (D-OENC)*: This method uses lossless compression of TST to reduce encoding overhead further. The basic idea is to reduce the number of bits required to encode each outlier. Instead of encoding actual interval values, we encode a signed number to indicate the difference between each outlier and the first majority class, i.e., $C1$. This signed number represents the difference

Algorithm 2: Interval Classification Algorithm

```

1 function intv_freq_count ( $I[s], H[s], used$ )
2    $used = 0$  /* consumed array space */
3    $packet\_count = 1$  /* number of packets */
4   /* generate interval frequency hash table */
5   for  $i = 0; i < s; i++$  do
6     /* only for IENC and OENC */
7     if  $used < payload\_limit$  then
8       for  $j = 0; j < s; j++$  do
9         if  $j > i$  or  $j == (s - 1)$  then
10           $H[j].value = I[i]$ 
11           $H[j].count = 1$ 
12           $used++$ 
13          break
14        else if  $i == 0$  then
15           $H[j].value = I[i]$ 
16           $H[j].count = 1$ 
17           $used++$ 
18          break
19        else
20          if  $H[j] == I[i]$  then
21             $H[j].count++$ 
22             $used++$ 
23            break
24      else
25         $packet\_count = 2$ 
26        break
27   /* only for IENC and OENC */
28   if  $packet\_count == 2$  then
29     generate the interval frequency hash table with  $s/2$ 
30   return  $H[s], used$ 

```

between the two intervals as a multiple of clock accuracy (one nanosecond). Figure 4(e) shows the packet format used with this encoding. For example, if an inter-sample interval $I[i]$ is an outlier, the TST entry corresponding to this outlier is $I[i] - I[C1]$, where $I[C1]$ is the inter-sample interval of class $C1$. Figure 5 shows that D-OENC’s packet payload size is reduced by at least 66% compared to *Baseline-8B* and 57% compared to *Baseline-6B*. This is a 9% reduction compared with OENC when all the outliers are unique. In addition, D-OENC hits payload constraint when more than 47% of the intervals are unique with 512-sample batches. Once it reaches the limitation, D-OENC simply splits the 512 samples into two packets. As Figure 5(b) shows, D-OENC’s worst-case scenario with a 512-sample batch consumes 1741 bytes. When split into two packets, each packet consumes 1229 bytes, well within the payload limit. This not only reduces the computation time significantly, but also provides a way for reconstructing the second packet if the first packet is lost.

C. Interval Classification Algorithm

We use the hash table as a simple and effective method to count the frequency of sampling intervals, as demonstrated in Algorithm 2. With this method, the average time to search for an element is $O(1)$, while the worst-case time is $O(n)$, where

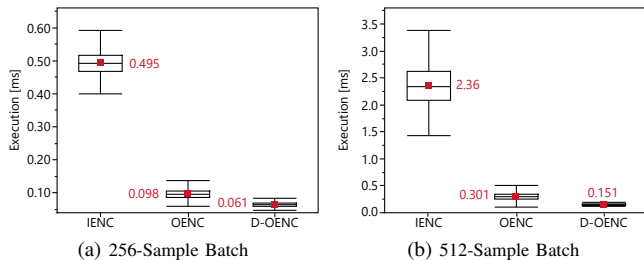


Fig. 6. Empirical evaluation of the execution time of the proposed encoding methods. The processor is an ARM-Cortex R4 operating at 160 MHz. The numbers represent mean values. IENC shows the largest variations because the chance of breaking a batch of samples into two packets is the highest with this encoding method. D-OENC achieves the minimum execution time among the three methods.

n refers to the number of samples in the batch [57], [58]. In our implementation, we only use stack memory to avoid the computation time uncertainty of dynamic memory. The variable *used* keeps track of the consumed array space by the number of classes. Line 5 shows that when the number of classes reaches the *payload_limit*, the algorithm breaks the loop and recomputes the hash table with half of the samples. This recomputing process happens with IENC and OENC only. After generating the frequency hash table $H[s]$, we use this table to compute the probability distribution of sampling intervals. Function `intv_freq_ranking()` is used to find the top seven classes— $C1$ through $C7$. The function computation time is based on the size of the consumed portion of $H[s]$, which is $O(\text{used})$. Only OENC and D-OENC use this function to rank the top seven classes.

D. Execution Time

Figure 6 shows the empirical evaluation of execution time on our node, which uses a 160 MHz ARM-Cortex R4 processor. The IENC computation time is more than 5x and 7x longer than OENC and D-OENC when using 256- and 512-sample batches, respectively. This is mainly because the number of interval classes impacts IENC’s computation time linearly, causing these large variations. Using 512-sample batches, IENC hits the packet payload limit when more than 12.5% of the intervals are unique (64 interval classes). This situation results in encoding the samples into two packets, which requires IENC to recompute the hash table. The OENC method performs a similar operation when more than 23% of the intervals are unique. However, D-OENC does not need to recompute the hash table when splitting into two packets is required.

As Algorithm 1 shows, during the Sampling Phase, each node performs sampling, encoding, packet preparation, and transmission sequentially. Therefore, a shorter encoding period is essential to achieve a stable and higher sampling rate. When the sampling rate is 100 ksps, these results show that IENC, OENC, and D-OENC result in missing about 49,

9, and 6 samples after collecting each 256-sample batch. When the batch size is 512, these values are 236, 30, and 15 samples. In summary, the results presented in Figures 5 and 6 confirm the superiority of D-OENC in terms of packet size efficiency and execution duration. When the batch size increases from 256 to 512, the execution time of D-OENC shows a 147% increase. Although using the smaller batch seems to be more efficient, we show in §IX that using the larger batch results in higher sampling efficiency.

V. REDUCING ENERGY CONSUMPTION DURING THE IDLE AND ALERT PHASES

In this section, we propose methods to reduce the energy consumption of Idle Phase and Alert Phase. We also propose methods to control the tradeoff between node responsiveness and energy efficiency level. In general, these methods can be used to develop 802.11-based WSNs that employ duty cycling to enhance their longevity.

A. Energy Efficiency Methods

We detail two energy efficiency methods in this section: *periodic association*, and *extended-period beacon reception*.

1) *Periodic Association*: In this method, each node periodically wakes up and associates with the AP, checks for a pending command from the server, and then either returns to an off mode (if no pending command) or transitions into the requested mode. The periodic association is triggered by a timer that fires every t_p seconds to perform the association. For this method, the energy consumed per second is computed as follows:

$$\bar{E} = \left(P_{asc} \times D_{asc} + P_{off} \times (t_p - D_{asc}) \right) / t_p \quad (1)$$

for $D_{asc} < t_p$

where P_{asc} refers to the average power consumed during the association process, and D_{asc} is the duration of the association process (the time it takes for the node to associate with an AP). P_{off} is power consumption during the off mode.

Although a node’s energy consumption can be reduced by increasing t_p , it is also possible to reduce this energy by improving the association process. We utilize two methods to reduce this energy. During the association process, a node sends probe packets on all channels to discover nearby APs. To avoid this overhead, we program the MAC address and channel of the AP into the node’s driver. This allows a node to directly send association request to the intended AP, thereby reducing probing overhead. We refer to this method as *Specific Association*. The second optimization is key computation offloading to the application processor. During the association process between a node and the AP, the node needs to establish a secure channel with the AP, and this process entails generating a Pairwise Master Key (PMK), which is a process-intensive task. Using the driver’s APIs, we offload

this key generation process to the application subsystem and then transfer the key to the wireless subsystem. We refer to this approach as *PMK Offloading*.

2) *Extended-Period Beacon Reception*: In this method, as soon as a node is turned on, it is associated with the AP. However, to ensure low-power operation while maintaining association, we employ Power Save Mode (PSM), which is the fundamental power saving mechanism supported by the 802.11 standard. With PSM, an associated node wakes up every 102.4 ms to receive a beacon packet from the AP. This periodic wake up allows the node to periodically receive beacon packets from the AP. When there is a buffered packet for a node, the AP sets a flag (per node) in the beacon packet to inform the node that it must request for the delivery of the buffered packet. Although the standard wake-up interval used by commercial APs is 102.4 ms, we can use a longer interval to reduce the overhead of beacon reception further. We refer to this method as *extended-period beacon reception*. To this end, we modified the PSM configuration in the driver (of nodes) to extend the default listen interval by a factor of l . We refer to l as the *listen interval coefficient*. With this method, the energy consumed per second is calculated as follows:

$$\bar{E} = P_{bcn} \times \left(\frac{D_{bcn}}{l \times 0.1024} \right) + P_{slp} \times \left(1 - \frac{D_{bcn}}{l \times 0.1024} \right) \quad (2)$$

where P_{bcn} and P_{slp} are power consumption during beacon reception and sleep modes, respectively, D_{bcn} is the duration of a beacon reception, and l is the coefficient of the listen interval used by the node. Note that D_{bcn} includes the duration a node waits in receive mode to receive a beacon, as well as the actual duration of beacon packet reception.

B. Transition Delay

As we showed in Figure 1, there exist delays when the system transitions from one phase to another. These delays were denoted as Idle Phase to Alert Phase (I2A) and Alert Phase to Sampling Phase (A2S). In this section, we study and reduce the duration of these delays for the two energy-efficiency methods explained above.

Using the periodic association method, although a larger value of t_p results in a deeper sleep phase, it also affects the nodes' responsiveness to commands. Assuming the command packet sent by the server can be generated at any time, the delay of command reception by a node is a uniform random variable in the range $[0, t_p]$ second. Using the extended-period beacon reception method, the delay of receiving the command is a uniform random variable in the range $[0, l \times 0.1024]$ second. Before presenting methods to reduce these delays, we introduce a definition of transition delay that makes it independent of command packet generation instance: *we define transition delay as the interval between*

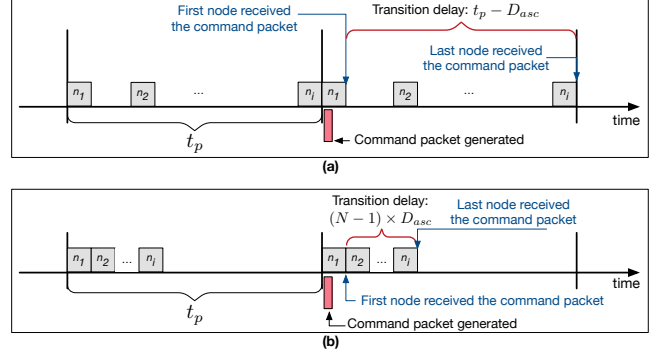


Fig. 7. Transition delay of periodic association method. (a) Without applying time synchronization, the transition period is $t_p - D_{asc}$. (b) By coordinating the association time of nodes, the transition period is reduced to $(N - 1) \times D_{asc}$ in a network including N nodes.

instances of the first and last node in the network receiving a command packet.

When using the periodic association method, Figure 7(a) shows that the transition delay is $t_p - D_{asc}$. For periodic association, the wake-up instance of the nodes can be coordinated if they are time-synchronized. Although it is desirable to allow all the nodes to associate with the AP concurrently, this method results in channel access contention, extends the association duration, and increases the nodes' energy consumption. An alternative approach is to time synchronize the nodes and serialize their associations, as Figure 7(b) demonstrates. For a system including N nodes, this method reduces transition delay to $(N - 1) \times D_{asc}$. For this method, a clock accuracy of up to a few tens of milliseconds would suffice. Each node synchronizes its clock with the server at each association instance.

For the extended-period beacon reception method, the server can issue the command right before all the nodes' wake-up instance. However, although each node wakes up every $l \times 0.1024$ second, their wake-up instances are not synchronized; therefore, transition delay equals $(l - 1) \times 0.1024$. This is demonstrated in Figure 8(a). We employ the following method to tackle this challenge. Once each node associates with the AP, the server informs the node about the sequence number of the initial beacon (b_{init}) packet, where $b_i = b_{init} + k \times l, k \in \mathbb{N}$ represents the beacon instances that must be received by all the nodes. Assume that a node associates with the AP and receives beacon number b_i . If $b_i = b_{init} + k \times l$, the node immediately enforces listen interval coefficient l . Otherwise, the node uses $l = 1$ until $\min(b_{init} + k \times l)$, where $b_i < b_{init} + k \times l$ and $k \in \mathbb{N}$. Then, the node starts enforcing the listen interval coefficient l . For example, in Figure 8(b), after the association of node n_1 is complete, this node keeps receiving beacons b_i through b_{i+3} . Once beacon b_{i+3} is received, the node enforces the listen interval coefficient l . In the worst case scenario where a node completes its association right after receiving beacon

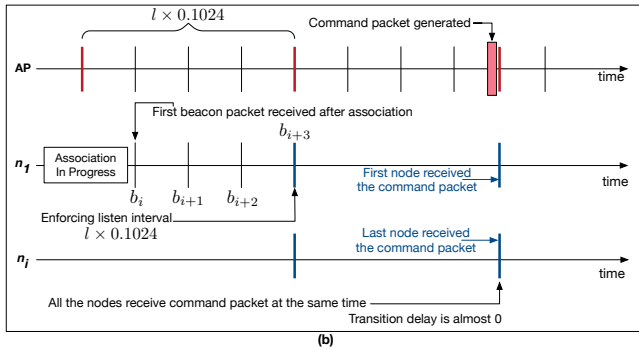
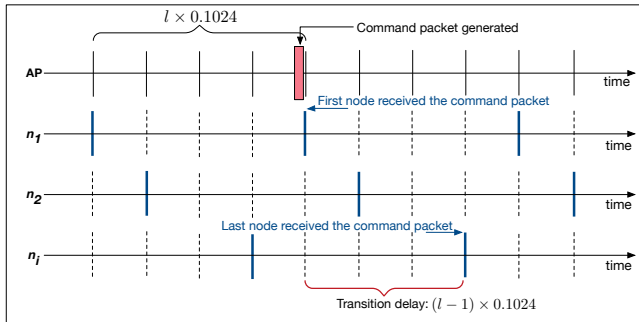


Fig. 8. Transition delay of extended-period beacon reception method. (a) Without synchronizing the wake-up instance of nodes, transition duration is $(l-1) \times 0.1024$. (b) Transition delay reduces to almost zero by coordinating the wake-up time of all the nodes.

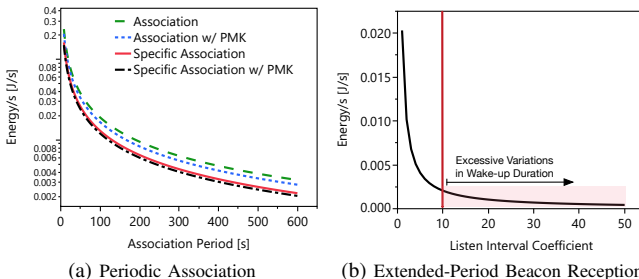


Fig. 9. Empirical energy evaluation of SoC. These results were collected in an interference-free environment.

$b_i = b_{init} + k \times l$, the node needs to receive l beacons before enforcing listen interval. With this method, the transition delay is almost 0.

C. Energy Comparison

Figure 9 shows the empirical measurement of energy consumption per second by the SoC (CYW54907) for the two proposed methods. For these results, we first measured the duration and energy consumption of various operations, and then used Equations 1 and 2. Since the energy consumed during the association process is high ($P_{asc} = 1.2\text{J}$ for Specific Association w/PMK), a long association period (t_p) is required to achieve a reasonable level of energy efficiency.

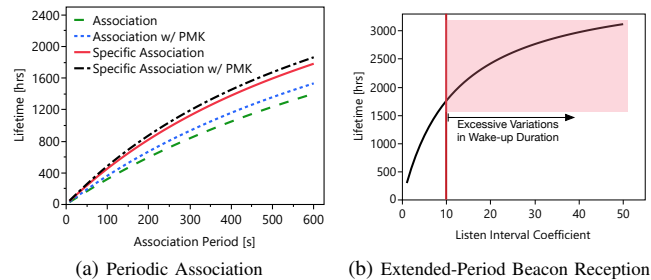


Fig. 10. Empirical evaluation of node lifetime. We assume battery capacity is 2500 mAh and only 80% of its capacity is usable. This evaluation takes into account the effect of all the on-board components that are required for proper operation of the SoC (§VIII-C2).

With beacon listen interval coefficient $l = 10$, the energy consumed per second is 0.00205 J, as Figure 9(b) shows. The same level of energy efficiency requires $t_p = 593$ when using the Specific Association w/PMK method, confirmed by Figure 9(a).

Although the extended-period beacon reception method seems to be preferred over the periodic association method, we noticed that as the listen interval coefficient increases, the sensitivity of nodes to beacon loss increases. Specifically, with a larger listen interval coefficient, a beacon loss results in longer energy consumed per beacon reception instance. For example, we noticed that $l > 10$ triggers this behavior with CYW54907 SoC. By investigating the 802.11 firmware, we observed that the link quality measurement algorithm requires receiving a certain number of beacons per unit time to measure link quality to the AP. Modifying these internal algorithms to ensure stable system performance for large listen interval coefficients may not be possible with various 802.11 transceivers. Therefore, in environments where beacon loss may happen due to interference or low link quality, the listen interval coefficient must be carefully adjusted based on the characteristics of the 802.11 transceiver used.

For the results in Figure 9, we only measured the energy consumed by the SoC. However, additional components on the board are required for the SoC to operate. As we discuss in §VIII, the battery gas gauge, buck-boost converter, and a 3.3 V regulator are required for the operation of the SoC in Idle Phase and Alert Phase. Considering the effect of these components (§VIII, Table I), we compute the lifetime of a 2500 mAh battery attached to a node. When computing lifetime, we also assume that up to 80% of the battery capacity can be used. Figure 10 presents empirical results for the two proposed energy-efficiency methods. We can observe the considerable effect of improving the efficiency of the association process on lifetime. For example, specific association w/PMK offloading enhances lifetime between 29% to 57%, compared to association.

D. Energy Efficiency Parameters

In this section, we study the configuration of energy-efficiency parameters. In particular, considering the energy efficiency methods given in §V, we discuss how t_p and l can be configured.

Based on the energy consumption models given in §V, the following inequality must hold to satisfy the energy-efficiency requirement:

$$E_{idl}(t_{idl}) + E_{i2a}(t_{i2a}) + E_{alt}(t_{alt}) + E_{a2s}(t_{a2s}) + E_{smp}(t_{smp}) < E_{bat} \times 80\% \quad (3)$$

$$\text{Subject to : } 1 \leq l \leq 10 \text{ and } D_{asc} < t_p$$

where $E_{idl}(\cdot)$, $E_{i2a}(\cdot)$, $E_{alt}(\cdot)$, $E_{a2s}(\cdot)$, and $E_{smp}(\cdot)$ are functions to compute the energy consumed during the Idle Phase, I2A transition, Alert Phase, A2S transition, and Sampling Phase, respectively. E_{bat} is the total available energy of the battery and we assume only 80% of the battery capacity can be used. In the rest of this section, we assume $E_{a2s}(t_{a2s}) = 0$ as we proved in §V. Considering the energy efficiency models given in §V, we extend the above Inequality 3 as follows:

$$\begin{aligned} & \underbrace{t_{idl} \times \left(\left(P_{asc} \times D_{asc} + P_{off} \times (t_p - D_{asc}) \right) / t_p \right)}_{\text{(a) Idle Phase}} + \\ & \underbrace{(l \times 0.1024) \times \left(P_{bcn} \left(\frac{D_{bcn}}{0.1024} \right) + P_{slp} \left(1 - \frac{D_{bcn}}{0.1024} \right) \right)}_{\text{(b) Alert Phase: Enforcing Listen Interval } l} + \\ & \underbrace{\left((N-1) \times D_{asc} - (l \times 0.1024) \right) \times \left(P_{bcn} \left(\frac{D_{bcn}}{l \times 0.1024} \right) + P_{slp} \times \left(1 - \frac{D_{bcn}}{l \times 0.1024} \right) \right)}_{\text{(c) Alert Phase: I2A transition of other nodes}} + \\ & \underbrace{P_{slp} \times \left(1 - \frac{D_{bcn}}{l \times 0.1024} \right)}_{\text{(c) Alert Phase: I2A transition of other nodes (continued)}} + \\ & \underbrace{(l \times 0.1024) \times \left(P_{bcn} \times \left(\frac{D_{bcn}}{l \times 0.1024} \right) + P_{slp} \times \left(1 - \frac{D_{bcn}}{l \times 0.1024} \right) \right)}_{\text{(d) Alert Phase: Enforcing Listen Interval } l \text{ by last node}} + \\ & \underbrace{P_{slp} \times \left(1 - \frac{D_{bcn}}{l \times 0.1024} \right)}_{\text{(d) Alert Phase: Enforcing Listen Interval } l \text{ by last node (continued)}} + \\ & \underbrace{t_{smp} \times \bar{E}_{smp}}_{\text{(e) Sampling Phase}} + \\ & < 0.8 \times E_{bat} \end{aligned}$$

Subject to : $1 \leq l \leq 10$ and $D_{asc} < t_p$ (4)

We detail this model as follows. We assume that the periodic association method is used during the Idle Phase, and the extended-period beacon reception is used during the Alert Phase. This is because the periodic association method can be used to achieve a deeper sleep mode. $E_{idl}(t_{idl}) = t_{idl} \times \bar{E}_{idl}$, where \bar{E}_{idl} is computed in Equation 1, as demonstrated in Equation 4(a). Once the first node transitioned into Alert phase, it takes $(N-1) \times D_{asc}$ seconds for the rest of the nodes to complete their transition. During this transition duration, the energy consumed by the node can be computed using Equation 2. However, note that the node may need up to $l \times 0.1024$ seconds before enforcing the listen interval l , as discussed in §V. The energy consumed in this mode is computed as $(l \times 0.1024) \times \bar{E}_{alt}$, where \bar{E}_{alt} is computed by Equation 2. Note that the value of l in Equation 2 must be 1. This is demonstrated in Equation 4(b). After enforcing the listen interval l , the energy consumed during $(N-1) \times D_{asc} - (l \times 0.1024)$ is computed in a similar manner using Equation 2, as demonstrated in Equation 4(c). Once all the nodes transitioned into the Alert Phase, the last node that has just transitioned may need up to $l \times 0.1024$ seconds to synchronize with all the nodes' wake-up time. The energy consumed during this duration is demonstrated in Equation 4(d). Finally, $E_{smp}(t_{smp}) = t_{smp} \times \bar{E}_{smp}$, where \bar{E}_{smp} is the energy consumed per second during the Sampling Phase. We will present this energy in §IX-C.

VI. PACKET CREATION AND PROTOCOL STACK PROCESSING

Compared to the 802.15 family of standards, the protocol stack of 802.11 is more complicated and introduces unique challenges in terms of packet processing delay and its effect on sampling rate and inter-sample interval. In this section, we propose methods to tackle these challenges.

A. Packet Processing Delay and its Effect on Sampling Rate

When samples and their timestamps are ready, there are three delay components incurred to transmit a packet: packet preparation, network stack processing, and packet transmission by the transceiver.

Both FreeRTOS [39], [40] and ThreadX [41], [42] require the application thread to create a packet data structure. This process, which we refer to as *packet creation*, entails buffer allocation from a pool available by the network stack. Next, the application payload is sent to the network stack to compute and add proper headers, including TCP/UDP, IP, and MAC. This process is referred to as *packet processing*. Finally, the frame is passed to the wireless subsystem for transmission. Since the SoC includes separate application and wireless subsystems, packet creation and packet processing tasks run on the application subsystem, and low-level packet transmission operations (e.g., carrier sensing, backoff) are handled by the wireless subsystem. Therefore, it is essential

to reduce the overhead of packet creation and processing to minimize their impact on the sampling task. In this section, we study the impact of three protocol stacks: LwIP [43], NetX [44], and NetXDuo [45]. LwIP is compatible with FreeRTOS, and the other two stacks work with ThreadX. Although both NetX and NetXDuo support UDP and TCP sockets, the major difference is that NetXDuo supports both IPv4 and IPv6 stacks. Considering the higher overhead of TCP, and since packets are transmitted over a single hop in our application, we use UDP. We assume that reliability is addressed by other means such as link-layer retransmissions.

Figure 11(a) compares the packet preparation delay of LwIP, NetX, and NetXDuo. The average packet creation delay is around $2.5 \mu\text{s}$ for LwIP and $0.5 \mu\text{s}$ for NetXDuo and NetX. The main cause of this difference is the memory allocation method used for packet buffers. With LwIP, the packet structure prepared in the application thread is copied to the network stack; whereas, NetX and NetXDuo provide a zero-copy method to prevent this overhead.

Once packet preparation is complete, the `packet_send()` API is called (cf. Algorithm 1). Simply measuring this API's execution time does not allow us to profile packet processing time by the network stack because, regardless of the network stack used, this API returns once the packet is delivered to the network stack. To tackle this challenge, we measure packet processing time as follows. We modified the network stacks to keep track of two events for each packet: (i) when the packet arrives in the network stack and (ii) when the packet is fully processed by the driver and is ready to be sent to the firmware. Figure 11(b) demonstrates packet processing delay. In this figure, using the name of a protocol stack refers to standard packet processing, which includes generating UDP, IP, and MAC headers. The results demonstrate that packet processing's mean latency with NetX and NetXDuo is about 65% lower than that of LwIP. One of the main reasons causing the lower performance of LwIP is that it performs multiple validation steps while the packet is passed through the stack. For example, LwIP checks if the socket is valid before further processing a packet. Also, both NetX and NetXDuo implement an enhanced UDP processing implementation to reduce its overhead [44], [45].

To reduce protocol stack processing overhead, we modified NetX and NetXDuo to *bypass UDP checksum generation*. These enhanced stacks are denoted as NetX-NC and NetXDuo-NC, where 'NC' refers to No Checksum. The results in Figure 11(b) show that bypassing UDP checksum reduces packet processing time of NetX and NetXDuo by 62% and 24%, respectively.

To further reduce packet processing delay, we fully bypass UDP processing. These protocol stacks are called NetX-R and NetXDuo-R, where 'R' stands for *raw*. With this enhancement, NetX-R and NetXDuo-R achieve $1.96 \mu\text{s}$ and $10.22 \mu\text{s}$ delay, respectively. In other words, the delay of

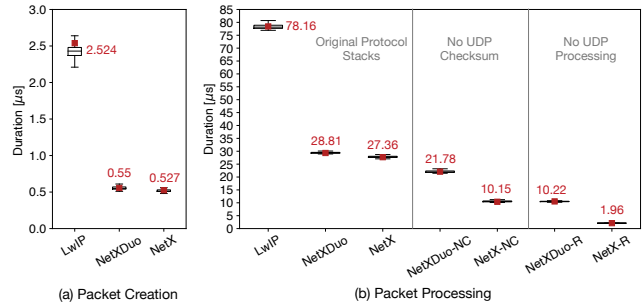


Fig. 11. Empirical evaluation of (a) packet creation, and (b) packet processing duration. The number on each box plot presents the mean value. NetX-NC and NetXDuo-NC refer to bypassing UDP checksum, where 'NC' stands for No Checksum. NetX-R and NetXDuo-R refer to *raw* socket processing, which means fully bypassing UDP layer.

NetX-R and NetXDuo-R are reduced by 92% and 64%, compared to NetX and NetXDuo, respectively. Considering the execution duration of these network stacks, when collecting 256-sample batches at 500 kbps, the packet processing delay of LwIP, NetX, and NetXDuo result in missing about 39, 13, 14 samples per packet processing, respectively. With NetX-R and NetXDuo-R, the number of missing samples is reduced to 1 and 5 samples per packet processing, respectively. *Considering the lower packet processing delay of NetX, we use this network stack in the rest of this paper.*

B. Impact on Sampling Stability

As mentioned earlier, the `packet_send()` API returns once the packet is delivered to the protocol stack. Therefore, when the node switches to sampling, the *network stack processing running in the background may disturb the sampling period*. In other words, the processor keeps switching between sampling and packet processing until the packet is fully processed. Figure 12 shows variations of inter-sampling intervals versus network stack processing type when sampling at 100 kbps. In these results, the node is collecting 60000 iterations of 512-sample batches. In this figure, the 'Sampling' label represents the case where no protocol stack processing is used. In other words, the Sampling results are collected on a node that only performs sampling, which is the same as Figure 3 presented in §IV-D. As Figure 12 demonstrates, the inter-sample intervals achieved by using NetX-NC and NetX-R are up to 42.05 and $25.39 \mu\text{s}$, respectively, which are significantly higher than Sampling results. These results confirm that running packet processing while sampling is in progress causes higher variations in inter-sample intervals.

To remedy this problem, we modified the NetX stack and converted the `packet_send()` API into a blocking call. *The new API returns when the packet passes through all the layers and is processed by the driver*. Therefore, sampling and protocol stack processing tasks run sequentially. These methods are named NetX-NC-B and NetX-R-B in Figure 12,

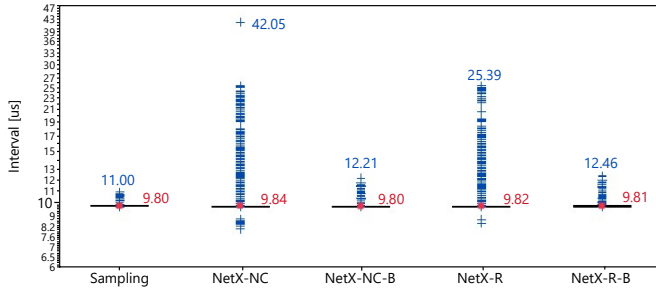
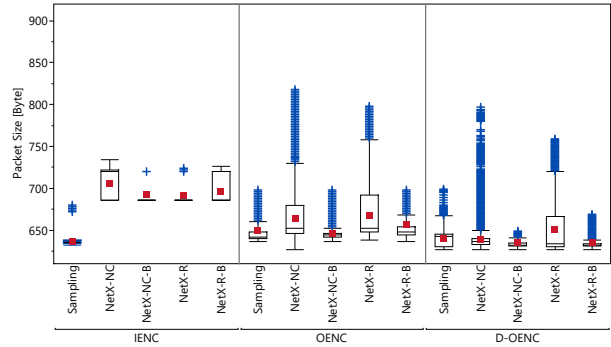


Fig. 12. Variations of inter-sample intervals when performing 60000 iterations of collecting 512-sample batches. The numbers on top of the outliers represent the maximum outlier value, and the numbers on the right side of each box plot represent the mean values. *Sampling* refers to the case where no packet processing task runs on the system. NetX-NC and NetX-R refer to *no UDP checksum* and *raw* packet processing, respectively. NetX-NC-B and NetX-R-B refer to the *blocking call* versions of packet processing using NetX-NC and NetX-R, respectively. The blocking call implementations reduce interval variations by up to 70%. Compared to Sampling, the higher variations of NetX-NC-B and NetX-R-B are caused by the communication between driver and firmware.

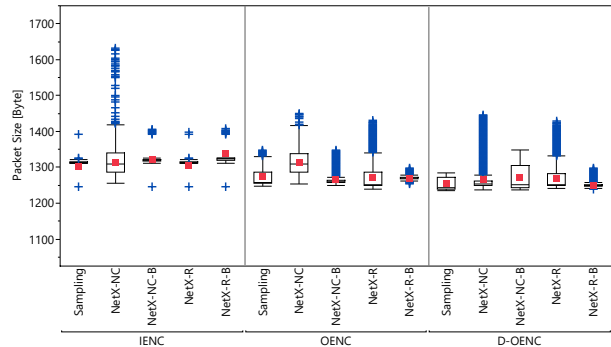
where 'B' refers to *blocking*. As the results show, for NetX-NC-B and NetX-R-B, the maximum inter-sample variation is dropped by 70% and 50%, respectively. Note that converting `packet_send()` to a blocking call does not mean that packets cannot be buffered. We provisioned a 200-packet buffer in the driver. Once a packet is fully processed by the protocol stack, the control returns to the sampling task if the buffer is not full. If the buffer is full, the packet processing API waits for the packet buffer to become available before resuming sampling.

Even with using a blocking call, the range of variations is still higher than Sampling. We identified that the driver-firmware interactions cause these outliers. The SoC we used in our node design has two processors, as discussed in §III. The packet exchange between the wireless and application processors is via Direct Memory Access (DMA). Once the driver completes processing a packet, it is sent to the firmware immediately or later. The delay of sending a packet to the firmware is because the firmware, which resides in the wireless subsystem, may be busy sending another packet. The sampling rate is affected due to initiating a driver-firmware communication through DMA requires attention from the application processor. Nevertheless, these variations account for less than 1% of inter-sample intervals.

As discussed in §IV-D, the higher the range of inter-sample variations, the larger the packet size. Although using the blocking call reduces the variations, we are interested in measuring packet size subject to the variations caused by driver-firmware communication and compare it to the Sampling case. Figure 13 shows the empirical payload size of the encoding algorithms on a node collecting 60000 sample batches at 100 kbps. The main observations are as follows. First, these results confirm that the packet size generated by IENC is higher than those generated by OENC and D-OENC.



(a) 256-Sample Batch



(b) 512-Sample Batch

Fig. 13. Empirical measurement of packet size using the three encoding methods with (a) 256-sample batches and (b) 512-sample batches. Both NetX-NC-B and NetX-R-B reduce packet size, and this reduction results in a lower bandwidth utilization. NetX-NC-B and NetX-R-B prevent concurrent execution of sampling and packet processing by implementing a blocking packet processing API.

For example, with 512-sample batches, the high variations of NetX-NC result in cases where packet size exceeds the MTU size of 1472 bytes. Second, the results show a higher number of outliers when using NetX-NC and NetX-R. Therefore confirming that the concurrent execution of sampling and packet processing tasks results in unnecessarily higher data rates and bandwidth waste.

VII. TIME SYNCHRONIZATION

Accurate analysis of the server's collected data requires establishing time synchronization across all the nodes and timestamping all the samples. In the proposed system, we achieve time synchronization by the periodic transmission of a broadcast time synchronization packet from the server to all the nodes. Each broadcast packet is sent once by the AP, and all the nodes receive this packet concurrently. When a node receives this packet, it modifies its internal timer by running a Time Synchronization Function (TSF) that adjusts the node's clock with the one received in the packet. The time synchronization packet's payload size is nine bytes, where

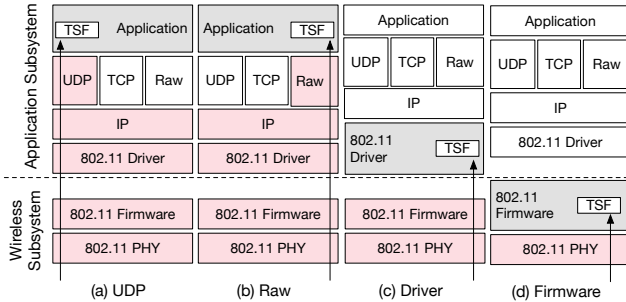


Fig. 14. The incoming broadcast packet used for time synchronization passes through all the shaded layers until it reaches the layer that includes TSF. The overhead of protocol stack processing drops from (a) to (d).

eight bytes is used for nanosecond time and one byte for packet type identification.

Although, in general, establishing time synchronization in single-hop networks is more straightforward than in multi-hop networks, the use of 802.11 standard introduces unique challenges. This section focuses on the delay of processing incoming packets as the leading cause of time synchronization error.

A. Packet Reception Delay

Considering LwIP, NetX, and NetXDuo, we study how protocol stack layers, from the 802.11 firmware up to the UDP layer, affect the delay of processing an incoming packet. We modified these network stacks and placed the TSF in different layers. Figure 14 shows these scenarios. Since the ultimate goal of time synchronization is to ensure all the nodes use the same clock value when adding timestamps to samples, we measured the time difference between two nodes immediately after processing the time synchronization packet. This experiment was repeated for over one million iterations. Figure 15 presents the empirical results. It is important to note that these results present the *difference* between the delay of processing time synchronization packets by the two nodes in our testbed. We detail these results as follows.

Bypassing UDP checksum in LwIP and NetX results in close to $30 \mu\text{s}$ error. With NetXDuo, however, the max error is close to $120 \mu\text{s}$. We identified this increase due to the higher processing overhead of NetXDuo caused by its IPv6 supporting feature. The results also show that, although using raw sockets entirely bypasses UDP layer processing, it does not reduce time synchronization error. The same observation is made even when the TSF is placed in the driver. These results indicate that the causes of processing time variability are located before the packet is delivered to the driver. In particular, *once subtracted across the two nodes*, the delay of memory allocation to the packet and processing it in the driver and upper layers is almost negligible compared to the delays caused before the packet arrives in the driver. As

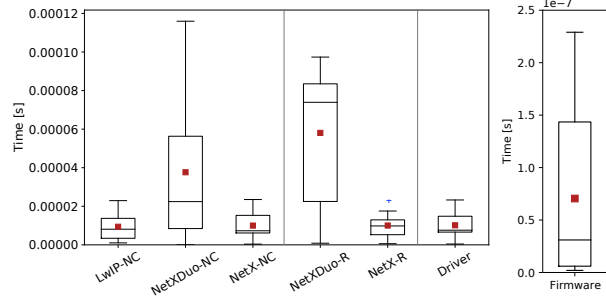


Fig. 15. Empirical evaluation of time synchronization error. When the TSF is implemented in the driver or a layer above it, the worst-case accuracy surpasses $20 \mu\text{s}$. When the TSF is implemented in the firmware, the worst-case accuracy is less than $0.25 \mu\text{s}$. These results confirm that firmware-level time synchronization is required to achieve sub- μs accuracy.

discussed in §VI, packet exchange between the wireless and application subsystems is via DMA. With this architecture, time synchronization error is caused by the instance interrupts are raised by the wireless subsystem of each node. Based on this observation, we moved the TSF to the firmware, run by the wireless subsystem’s processor. Thus, time synchronization happens when the packet is received, but before it is transferred to the application subsystem via DMA. With this enhancement, as Figure 15 shows, the maximum error drops to less than $0.25 \mu\text{s}$. This accuracy is sufficient to maintain time synchronization accuracy for sampling rates up to 1 Msps.

B. Periodic Time Synchronization

The server must periodically transmit a time synchronization packet to ensure that the nodes’ clocks do not deviate beyond a specific limit. Determining the proper period depends on the clock stability of the nodes’ processor. The processor’s clock frequency stability, denoted as ν , varies based on changes in temperature, voltage, output load, and aging. Frequency stability is typically expressed in parts per million (*ppm*). Peak frequency variation can be presented as $d_f = f \times \nu$, where f is processor frequency [59]. The maximum time difference between two nodes per second can be expressed as $d_t = \frac{1}{(f-d_f)} - \frac{1}{(f+d_f)}$. The CYW54907 [52] used in our node design runs at 160 MHz and its $\nu = \pm 2.5 \text{ ppm}$. Therefore, its peak frequency variation is $d_f = 400 \text{ Hz}$, and the maximum timing error per second between two nodes is $d_t = 5 \mu\text{s}$.

Figure 16 demonstrates the maximum time deviation between two nodes (excluding the initial error) versus the time synchronization period. The maximum synchronization error immediately after processing the time synchronization packet is less than $0.25 \mu\text{s}$. When sampling at 500 ksps, a time synchronization error of less than $1 \mu\text{s}$ allows the server to correlate the samples, which are collected every $2 \mu\text{s}$. Therefore, the error accumulated over time must be limited

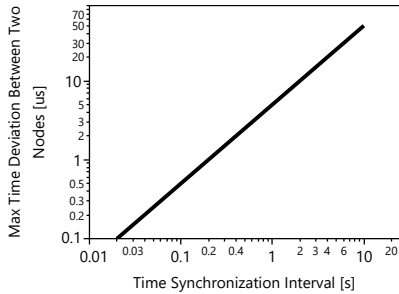


Fig. 16. Maximum time difference between two nodes versus time synchronization period. This figure does not take into account the initial time synchronization error caused by processing time synchronization packet.

to less than $0.75 \mu\text{s}$. As Figure 16 shows, this requires a time synchronization period of less than 150 ms. For 100 kbps, the error accumulated over time must be limited to less than $9.75 \mu\text{s}$, which requires a time synchronization period of 1.95 s.

VIII. HARDWARE DESIGN

The primary hardware design considerations are low-power consumption, supporting high sampling rates, and providing a small form factor. In this section, we discuss our node design. We also present the node's power consumption considering the minimum number of components that must be operational during the Idle Phase and Alert Phase.

At a high level, our proposed node design consists of three main components: (i) *processor and wireless transceiver* unit, referred to as SoC; (ii) *sensing* unit; and (iii) *power management* unit. Figure 17 presents the block diagram of a Sensifi node and Figure 18 demonstrates our prototype. A node includes components (such as current monitor, battery gas gauge, and probe pins) to facilitate performance study and the adaption of this design for various applications. Without these components, the size of a production-quality node can become significantly smaller.

The SoC is used to collect data from the sensing unit, construct data packets, send packets to an AP, and control the sensing and power management units. The sensing unit is responsible for measuring acceleration forces and converting analog measurements to digital data. The power management unit supplies all the components with a stable power source, provides an accurate reference voltage to the sensing unit, measures the node's power consumption, and protects the node from under-voltage discharge.

A. SoC: Processor and Wireless Transceiver

As discussed in §III, our design is based on CYW54907 [52] and supports 802.11ac rates. Our design is also compatible with CYW43907 [60], which supports 802.11n.

Although 802.15.4 and Bluetooth are the prevalent communication standards used in WSNs, the communication

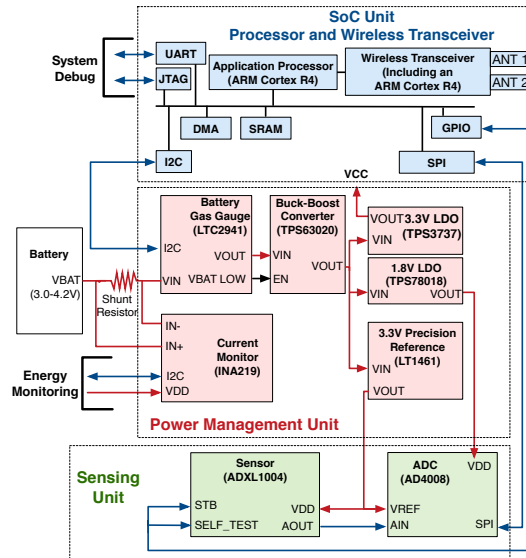


Fig. 17. The block diagram of a Sensifi node. Depending on the operational phase of the node, some components of the power management unit can be turned off. For example, during the Idle Phase and Alert Phase, only the gas gauge, buck-boost converter, and the 3.3 V LDO need to be active.

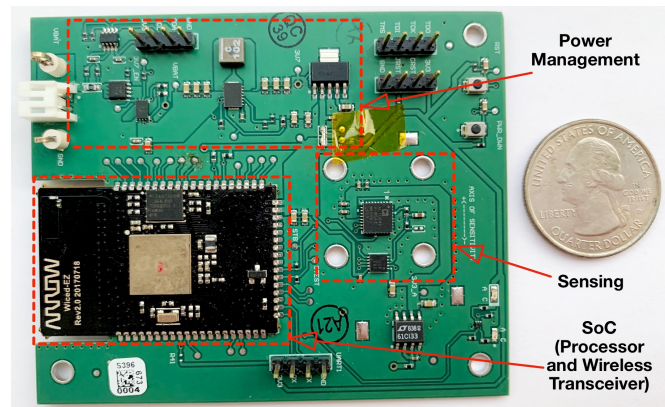


Fig. 18. A Sensifi node prototype. The prototype includes components (such as current meter and gas gauge) that are used for developmental purposes. These components can be removed to obtain a smaller, lower-power node design.

standard we used in this work is 802.11, considering the following reasons. Large-scale vibration testing requires sending high-rate sensory data from a large number of nodes to a server [12]. Therefore, it is essential to select a wireless protocol that can support the expected data rate. Both Bluetooth classic and Bluetooth Low Energy (BLE) support communication range around 50 m, depending on their transmission power. However, Bluetooth classic is not suitable for large-scale, ultra-high-rate applications because it only supports seven slave devices, and its total available rate is 2.1 Mbps. Although BLE supports connecting a large number of devices to a master, its maximum achievable data rate is 1.37 Mbps.

Also, its maximum allowable packet size is 27 bytes, and this limitation reduces the efficiency of packet encoding, as discussed in §IV. While BLE is known as a very low-power wireless standard, recent studies reveal that from the physical layer point of view, 802.11 is more energy-efficient than BLE. For example, [61] shows that the required energy per bit for BLE and 802.11 are 275 - 300 nJ/bit and 10 - 100 nJ/bit, respectively. Since the higher energy consumption of 802.11 is caused by connection establishment and maintenance, we proposed methods in §V to lower these overheads.

B. Sensing Unit

The sensing unit consists of two components, a Micro-Electro-Mechanical Systems (MEMS) accelerometer and an ADC. The details of these components are discussed as follows.

1) *Sensor*: As discussed in §II, vibration test requires accelerometers to measure frequencies from 10 Hz to 10 kHz. However, most accelerometers are geared toward the analysis frequency tilted to one side of the frequency spectrum. In addition to accuracy, the sensor must be low-power, low-cost, and available in a small form factor. Thus, choosing the proper accelerometer is a crucial step to provide the required measurement accuracy, rate, and power efficiency. Considering these requirements, capacitive accelerometers are suitable for measuring static and dynamic accelerations, offering linearity, showing high output stability, and low cost. The sensor used in our node design is ADXL1004 [62], a MEMS capacitive accelerometer with a measurement range of ± 500 g-force and capable of measuring frequencies of up to 24 kHz. Its maximum power consumption is 5 mW and its noise range is up to $125 \mu\text{g}/\sqrt{\text{Hz}}$. Sensor sensitivity is 2.64 mV/g with an input voltage of 3.3 V. To achieve this sensitivity, we use a precision voltage rail for the sensor's power input to provide a low variance ($\leq 1\%$) across temperature and node-to-node.

2) *ADC*: The primary considerations regarding the choice of ADC are resolution, sampling rate, energy efficiency, signal conditioning, and digital interface. Since the highest sampling frequency measured by the sensor is 24 kHz, according to the Nyquist theorem, the sampling rate must be at least 2×24 kHz. The sensor has 2.64 mV/g sensitivity with input voltage 3.3 V. Although a 12-bit ADC with 1.6 mV resolution and input voltage of 3.3 V is sufficient to acquire the sensor's output accurately, we use an ADC that provides higher resolution and is capable of sampling at considerably higher rates. With this design, the ADC can interface with different types of sensors and be used in applications with higher demands. Specifically, our design includes a 16-bit AD4008 [63] that supports a maximum sampling rate of 500 ksp/s and is accessible through a SPI interface. To interface the ADC with the SoC, we developed a custom SPI bus driver. To this end, in addition to the datasheet,

we used the FPGA-based evaluation board and Windows-based software available for this ADC to fully understand its timing requirements and implement a driver that allows us to sample at 500 ksp/s. AD4008 requires a reference voltage of 3.3 V to provide an output resolution of 0.1 mV and accurately measure the sensor's output. The high-Z mode provided by AD4008 is intended to mitigate nonlinear charge kickback effects at the start of each acquisition phase when the sampling capacitors connect to the input voltage. In addition, the high-impedance mode allows us to simplify the complexity of the node design by not requiring an input signal buffer to drive the ADC. This means that the analog voltage output from the sensor, which follows an RC low-pass filter in our design, can be directly connected to the analog inputs of the ADC.

C. Power Management Unit

The power management unit consists of five components: a battery gas gauge [64], a bucket-boost converter [65], two LDO regulators [66], [67], a precision reference [68], and a current monitor [69]. In this section, we detail the design and empirical analysis of the energy consumption by this unit.

1) *Components*: In Figure 1, each node operates in various modes, ranging from Idle Phase, in which there is minimal current draw, to Sampling Phase, where hundreds of milliamps may be consumed. Therefore, the power management unit must be capable of operating over a wide load profile. Our design uses a Lithium-Polymer (LiPo) battery, which has the highest energy density compared to other rechargeable batteries such as Nickel-Cadmium (NiCd) and Nickel-Metal Hydride (Ni-MH). Since the LiPo battery's nominal voltage is close to the on-board components' voltage requirement, the voltage regulating stages are reduced and efficiency is improved.

The gas gauge is used to protect the battery from under-voltage discharge and monitor the battery's remaining charge. The gas gauge is placed after a PMOS transistor for reverse voltage protection. The $\overline{\text{AL}}/\text{CC}$ pin of the gas gauge is connected to the 3.7 V regulator's enable pin to perform low-battery detection. When the battery runs below the 3 V threshold, the gas gauge drives the $\overline{\text{AL}}/\text{CC}$ pin low and disables the regulator. Note that the gas gauge is not a critical component and may not be required for a production-quality node design.

The bucket-boost converter (TPS63020) is part of the node's main voltage rail and feeds into the cascaded linear regulators. By simulating performance across the design input voltage range and load currents up to 500 mA, the bucket-boost converter shows an efficiency range between 88% at light current load and up to 94.5% for the maximum current load [65]. However, the bucket-boost converter introduces a switching noise that affects other sensitive analog components when the performance efficiency reaches 90%. To reduce the noise and provide a steady voltage output,

TABLE I
CURRENT CONSUMPTION BY THE POWER MANAGEMENT UNIT

	Active Component's Current (mA)					Total Current (mA)
	Battery Gas Gauge	Buck Boost Converter	3.3V LDO	1.8V LDO	3.3V Ref	
Idle/Alert Phase	0.1	0.105	0.297	-	-	0.502
Sampling Phase	0.1	0.105	0.297	0.872	0.07	1.444

our design uses TPS3737 [66] 3.3 V and TPS78018 [67] 1.8 V LDO regulators. The 3.3 V regulator provides a stable voltage for the processor and wireless transceiver unit, and the 1.8 V regulator provides a stable voltage for the ADC. Since AD4008 and ADXL1004 only consume a maximum of 2 mA during sampling, the impact of dissipated power loss for the 1.8 V LDO regulator is negligible.

Our design uses a LT1461 [68] to provide an extremely constant voltage reference that is resistant to temperature, noise on the supply rail, and process variations [70]. We connect the LT1461 to the ADXL1004 and AD4008 to prevent the risk of switching noise or voltage ripple, thereby reducing measurement inaccuracies. It can also deliver up to 50 mA load currents, and the output voltage is guaranteed to be within $\pm 0.08\%$ of the nominal value with a temperature drift of only 12 ppm/ $^{\circ}\text{C}$. To reduce power consumption during the Idle Phase, we use transistor switches to turn off the supply voltages of the ADXL1004 and AD4008. For developmental purposes and to eliminate the need to use an external power meter, an INA219 [71] is used for in-circuit power measurement.

2) *Energy Consumption*: We used a high-precision Digital Multimeter (DMM) [72] to study the power consumed by the components of the power measurement unit. Table I presents the results. During the Idle Phase and Alert Phase, both the ADXL1004 and AD4008 are completely turned off, and only the SoC needs to be powered. Table I shows that the current consumption of the power management unit during these phases is $502 \mu\text{A}$. The results we presented earlier in Figure 10 (§V-C) show the power consumed by the power management unit and SoC when comparing the periodic association and periodic beacon reception methods to enhance the energy efficiency of Idle Phase and Alert Phase. During the Sampling Phase, the sensor and ADC must be turned on as well. Due to the activation of the 1.8 V LDO and the 3.3 V reference voltage, the power consumption of the power management unit increases to 1.444 mA. We will present the overall energy consumption of a node during Sampling Phase in §IX-C.

IX. OVERALL SYSTEM EVALUATION

In this section, we evaluate the overall performance of the proposed system in terms of sampling rate (§IX-A), data

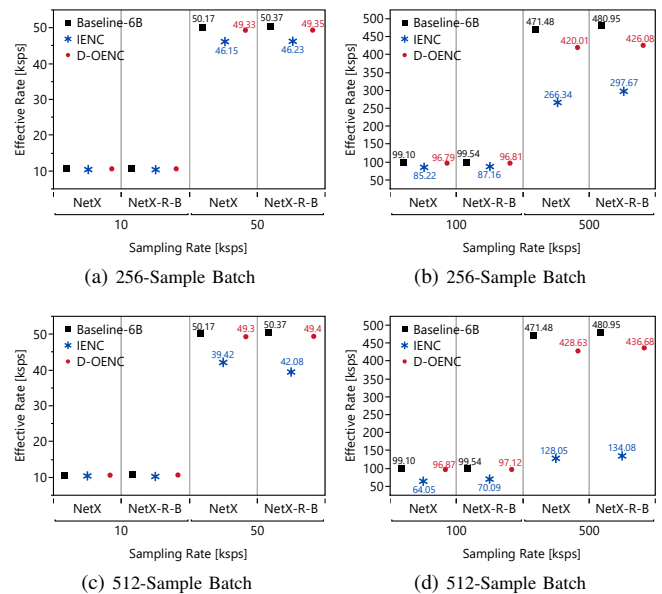


Fig. 19. Empirical measurement of *effective rate* for (a) and (b): 256-sample batches, and (c) and (d): 512-sample batches. The effective rate is the actual number of samples collected per second by a node. Note that the number of samples per packet when using Baseline-6B is always 183, independent of batch size. NetX refers to the default protocol stack, and NetX-R-B refers to the blocking call implementation of raw packet processing.

generation rate (§IX-B), and energy efficiency (§IX-C).

A. Effective Sampling Rate and Data Rate

Each node switches between sampling, packet encoding, packet creation, and packet processing during the Sampling Phase. In this section, we evaluate the overhead of the last three tasks on *effective rate*, defined as the actual number of samples collected per second by a node. Effective rate is measured as the actual number of samples received per second by the server. Figure 19 shows the empirical evaluation of the effective rate. We also measure wireless communication rate per node by using a wireless sniffer that captures all the packets exchanged between the node and AP. Figure 20 presents the empirical measurement of wireless communication rate for the same scenarios given in Figure 19.

Both Figures 19 and 20 include Baseline-6B, which represents the case where no encoding is applied on timestamps (§IV-B). Note that the number of samples per packet when using Baseline-6B is always 183, independent of batch size. As Figure 19 shows, we observe that the sampling rate achieved by Baseline-6B is closer to the target rate, compared to the cases where encoding is applied. This is because packet encoding introduces a processing time that causes sampling interruption. However, as Figure 20 shows, the data rate generated per node is considerably higher when using Baseline-6B. For example, when sampling at 500 kpsps, the sampling rate of D-OENC is 10% lower than that of

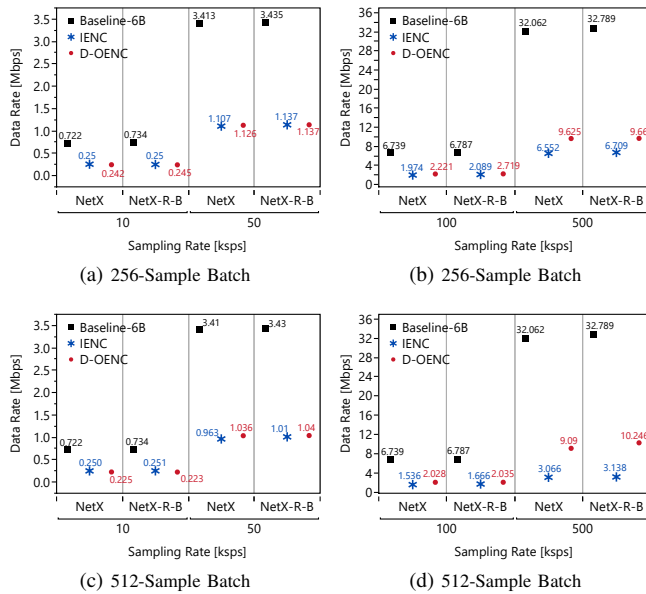


Fig. 20. Empirical measurement of wireless communication rate. The data generated per second by a node includes samples, timestamps, packet encoding data, and packet headers. Note that the number of samples per packet when using Baseline-6B is always 183, independent of batch size.

Baseline-6B (Figure 19(d)), whereas, the data rate generated by Baseline-6B is 220% higher (Figure 20(d)). Regardless of the channel access mechanism, the significantly higher data rate of Baseline-6B increases the number of APs required to ensure the bandwidth and reliability requirements of communication are met. Also note that for sampling rates less than 500 kbps, the effective rate achieved by D-OENC is almost the same as the target rate, but the amount of data generated by Baseline-6B is considerably higher.

As the sampling rate increases, the duration needed to collect a batch drops, but the overhead of encoding and packet processing remains unchanged; thereby, the effective rate drops as the sampling rate increases. With D-OENC, although the results in §IV-D demonstrated a 147% increase in processing time when switching from 256- to 512-sample batch, the results here show an almost similar performance for the two batch sizes. There are two reasons for this observation: First, packet processing overhead halves when the batch size doubles. Second, due to the SPI bus initialization time, the time it takes to collect 512 samples consecutively is less than collecting this number of samples in two 256-sample batches. In summary, by using D-OENC and NetX-R-B, we are able to collect up to 436 kbps when the ADC operates at 500 kbps, as Figure 19(d) shows. With IENC, however, we observe a considerably lower effective rate when comparing the smaller and the larger batch sizes, i.e., Figures 19(a) and (b) against (c) and (d). Based on the results presented in §IV-D, increasing the batch size from 256 to 512 exhibits a 376% increase in the execution time of IENC. This

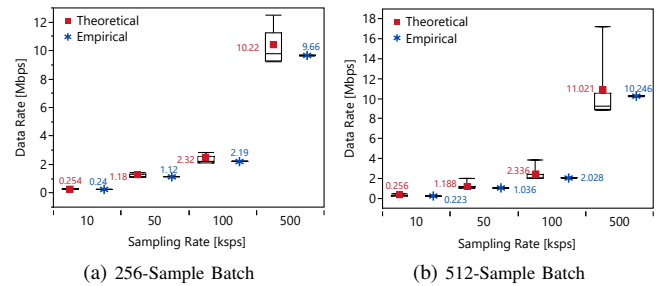


Fig. 21. The amount of data (samples, timestamps, and packet headers) generated per second by a node using D-OENC and considering theoretical and empirical variations of inter-sample intervals. The data rate variations are caused by the number of classes in each batch of samples. For the theoretical results, we assume the minimum number of classes is eight and the maximum number of classes is the number of samples in a batch minus one ($s - 1$).

significant increase in encoding time dominates the overheads caused by packet processing and SPI bus initialization.

These results also show the effect of network stack on both effective rate and data rate. Compared to NetX, using NetX-R-B results in faster packet processing, thereby increasing the effective rate. On the other hand, since NetX-R-B bypasses UDP processing, the packets do not include the UDP header, hence reducing the amount of data generated per second. For example, when sampling at 500 kbps, Figure 19(b) shows that using D-OENC with NetX-R-B increases the number of samples collected per second by about 6000, compared to NetX. This comes at 0.025 Mbps increase in data rate, as Figure 20(b) demonstrates. With IENC, Figure 20(b) shows that sampling rate increases by about 31000, and this causes 0.157 Mbps increase in data rate.

B. Theoretical versus Empirical Data Generation Rate

To study the potential effects of various factors such as ADC and concurrent processes on sampling rate consistency, in this section we theoretically evaluate the amount of data generated per node. We assume the minimum number of classes is eight and the maximum number of classes is batch size minus one (i.e., $s - 1$). We also compare the theoretical results with empirically collected data. For this study, we D-OENC and NetX-R-B.

Figure 21 presents these results. We observe that the range of theoretical data rate is higher for 512-sample batches. This means that in applications where sampling interval is affected by factors such as running concurrent processes, variations in processor-ADC communication rate, or ADC's sample conversion time inconsistency, using smaller batches reduces the overhead of timestamp encoding. The empirical results also show a tighter distribution compared to theoretical data, demonstrating that most inter-sample distributions are within a few inter-sample classes.

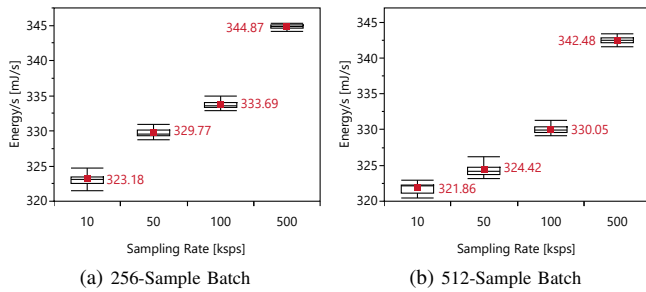


Fig. 22. Empirical measurement of energy consumption during the Sampling Phase. While the effective rate of the 512-sample batch size is higher (Figure 19), its energy consumption is lower because of the lesser overhead of packet processing and transmission.

C. Energy Consumption During Sampling Phase

We presented the energy consumed per second during the Idle Phase and Alert Phase in §V and §VIII-C2. In this section, we measure the energy consumption of a node that uses D-OENC and NetX-R-B during the Sampling Phase. Figure 22 presents the empirical measurement of energy consumption per second by a node for various sampling rates. As we increase the sampling rate from 10 kbps to 500 kbps, the energy consumed per second increases by 6.7% and 6.4% when using 256- and 512-sample batches, respectively. The higher energy consumption when using 256-sample batches is due to the higher packet header overhead caused by sending more packets. Also, with the smaller batch size, packet processing overhead increases and the number of switching between reception and transmission mode doubles.

We measured the power consumption of sensing and power management units separately and identified that these two components consume only 4.2% of the total power. As mentioned in §II, spacecraft vibration testing requires the sensor nodes to operate for 20 to 40 minutes during the Sampling Phase. Assuming that only 80% of a 2500 mAh battery can be used, based on our measurements, each node consumes 1.55% and 3.11% of the battery capacity when sampling at 500 kbps for 20 and 40 minutes, respectively. The remaining battery capacity is consumed before the Sampling Phase starts, i.e., during the Idle Phase and Alert Phases. Using the energy models given in §V, for example, when t_{idle} equals two weeks and $N = 100$, the values that satisfy the above inequality are $t_p = 57$ seconds and $l = 1$.

X. RELATED WORK

WSNs reduce the installation and maintenance costs of applications such as structural monitoring [30], [73], [74], machine health monitoring [4], [75], space applications [50], [76], and natural hazard monitoring [5], [77]. These systems are usually built on top of the 802.15 standards. This is because these standards offer low energy consumption, low cost, ease of integration with various microprocessors, and

the simplicity of configuring and customizing physical layer and MAC parameters [15], [30], [32], [50], [78]. However, the existing SHM systems do not support ultra-high-sampling rate. Instead, they either focus on the networking and energy efficiency aspects of multi-hop communication, or propose methods for distributed processing and data aggregation [35]. For example, Alves et al. [35] proposed a distributed system where sensor nodes entirely do the decision making. Their decentralized data processing reduces network traffic and provides real-time response to alert potential damages to wind turbines. Their system supports a sampling rate of 100 Hz. Although distributed processing can be leveraged to reduce the communication rate, not all the applications can benefit from this method. The applications that require long sampling duration [22] or raw sample collection across nodes [79] require centralized processing to enhance analysis accuracy and reduce the processing burden of nodes. In centralized processing applications that require a high sampling rate, wireless data transmission causes interruptions in the sampling task [8]; hence, we observe that existing works employ a non-live data collection strategy. For example, Kim et al. [22] proposed a multi-hop WSN composed of 64 nodes, each sampling at 1 kbps. Each node stores the collected samples in its local storage, and the saved data is then sent over 802.15.4 links. Dodson et al. [50] proposed *Martlet*, a node design for high g-force impact testing. Their primary contribution is developing an interface board to sample at 100 kbps and provide signal conditioning. The accelerometer's bandwidth is up to 10 kHz and its measurement range is ± 210 g-force. The collected data is stored in the node's RAM until a total of 16000 samples are collected. When requested, the data is sent over 802.15.4 links. Araujo et al. [23] proposed a WSN supporting 3906.25 sps. Each node is equipped with two wireless transceivers: 802.15.4 and 802.11. Considering the lower protocol stack delay of 802.15.4 compared to 802.11, they used the 802.15.4 standard to time synchronize the nodes. Collected samples are saved into a removable memory card, and once sampling is finished, the saved data is transferred to a server over 802.11 links. Mechtov et al. [79] proposed a centralized WSN that can support sampling rate at 250 sps. The system performs sampling for 60 s until the local storage is filled, and then transfers the data to the server using 802.15.4 links. Valenti et al. [21] proposed a low cost SHM for building monitoring. The system uses a cluster topology where each node transmits raw data to its cluster head, and the server collects the data from the cluster heads. The sensor nodes perform sampling at 4 kbps for 20 minutes until the local storage is full, and then transfer the data with a local timestamp to the cluster head. The cluster head is responsible for collecting GPS timestamps and sending all the data to the server over 802.15.4 links. Girolami et al. [80] proposed an 802.11-based SHM using Free-RTOS for monitoring building structures. The system samples at 25.6 kHz and then sends the average

of the collected data at a rate of 100 Hz. The microcontroller uses DMA for data transfer from ADC to the memory with double buffer configuration to improve the data transfer time. However, they did not provide an empirical evaluation of the actual sampling rate. The sensor nodes transfer data over 802.11 links after the local memory is filled with 100 seconds of measurement samples. Due to the non-live data transfer, each sensor node requires time synchronization with a Network Time Protocol (NTP) server to generate an accurate timestamp. However, time synchronization with the NTP server introduces an extra processing overhead. These works do not address the requirements of ultra-high-rate applications where data must be transferred to a central repository in a live manner. Specifically, the sampling and data rates we provided in this paper are significantly higher than those supported by the reviewed works.

The impact of writing to flash storage on sampling rate stability was studied in [22]. They showed that when sampling at 5 ksp/s, sampling jitter is increased by 10 μ s. They argued that a multi-processor node design is required to tackle this challenge. Dai et al. [81] considered a SHM system where each sample is written to a flash storage card. They demonstrated that the process of sample collection and writing to a memory card reduces the sampling rate. To address this problem, they used the DMA controller to directly transfer data from ADC to SRAM. In the end, the user can request for wireless transfer of the collected samples. Their work, however, presents performance enhancement in terms of processor cycles and not the actual sampling rate achieved. Phanish et al. [32] also used DMA to enhance sampling rate stability. Specifically, each sampling round collects and transfers 16 samples to SRAM via DMA. Then, each batch of samples is sent as one packet. Compared to our work, none of the existing works studied the effect of packet preparation and transmission on sampling rate.

Since processors' energy consumption is usually lower than that of wireless transceivers, data compression is another method used by the existing works to reduce the amount of data sent by each node and enhance energy efficiency. Considering the small packet sizes allowed by the 802.15.4, Islam et al. [38] argued that providing IP compatibility by using the 6LoWPAN adaptation layer requires compression. They proposed a payload compression method using an arithmetic coding algorithm and evaluated efficiency by comparing the data compression ratio, memory consumption, and compressed data size against Huffman coding. The result showed that the arithmetic coding has a much higher compression rate than Huffman coding when the original sample data size is more than 512 bytes. However, since the arithmetic coding algorithm has zero error tolerance when an error occurs, it is impossible to locate the error; therefore, the entire dataset is discarded. Depending on the number of encoding symbols, the arithmetic coding has a finite precision limitation for the sampling data. The accuracy of the sampling data is reduced

when the encoding symbols reach their precision limitation. Also, the impact of compression on processor utilization and sampling rate stability has not been evaluated.

The benefits of using 802.11 for building high-rate, energy-efficient WSNs have been studied recently. Abedi et al. [61] showed that at the physical layer, the energy consumption of 802.11 is 10 - 100 nJ/bit, while the range is 275 - 300 nJ/bit for BLE. They also argued that the overall energy consumption of 802.11 is higher than BLE due to connection establishment and maintaining connection. Tamarin et al. [82] evaluated the suitability of 802.11n in industrial applications from its physical layer point of view. Considering the higher header overhead of 802.11n compared to 802.11g, the former standard has a shorter transmission duration for packets longer than 224 bytes. Also, when backward compatibility is not necessary, using the Greenfield preamble reduces physical header overhead. They also evaluated the effect of Guard Interval (GI), Space-Time Block Coding (STBC), and Low-Density Parity-Check (LDPC) to enhance link reliability. Luvisotto et al. [14] provided an overview of the requirements of industrial wireless networks. They also studied the suitability of 802.11's physical layer to address some of the requirements of industrial communication systems compared to cellular and 802.15 networks. Yu et al. [83] proposed an 802.11-based WSN to monitor potential damages to bridge parts while they are being lifted and mounted. The proposed solution uses the 802.11b/g standard. The sampling rate of each node is 100 sp/s, each packet contains 80 samples, and the size of each sample is 16 bits. They used TCP/IP protocol stack to simplify data collection and interfacing with a PC.

Several works focus on addressing the challenges of real-time data transmission, especially in control systems. For 802.15.4 networks, this primarily entails proposing real-time scheduling methods. Since the 802.11 network protocol stack is more complicated than 802.15.4, various modifications to the stack have been proposed to replace its built-in Carrier-Sense Multiple Access (CSMA) mechanism with Time-Division Multiple Access (TDMA). Bartolomeu et al. [84] addressed the challenges of transmitting real-time packets in the presence of non-real-time traffic generated by other stations. To grasp the channel, real-time transmissions are preceded with jamming signals that are long enough to inform non-real-time stations about channel occupancy. Their results confirmed the protection of real-time 802.15.4 traffic against the contention generated by other 802.15.4 or 802.11 stations. Wei et al. [36] proposed RT-WiFi, a TDMA-based WiFi network to achieve a maximum of 6 kHz sampling rate. They argued that the Distributed Coordination Function (DCF) used by the 802.11 standard to arbitrate channel access results in non-deterministic packet delivery delay. They modified the driver and mac80211 module of the WiFi stack to receive transmission schedules from a central controller that assigns unique, non-overlapping time slots to nodes. Using three 802.11g nodes connected to an

AP, they showed that 99.98% of the packets are delivered within 500 μ s slots. They also evaluated system performance in a gait rehabilitation application where a mobile assistive robot and a smart shoe collect and transmit samples at 100 Hz and 1 kHz, respectively, and the controller replies at 100 Hz. Their work, however, does not address the challenges of scalability, high-rate transmission, and energy efficiency. Dombrowski and Gross [85] proposed EchoRing, a distributed and deterministic channel access method to enhance the reliability of using token-ring for channel access arbitration. Their measurement environment consists of five nodes, and using a software-defined radio operating in a 10 MHz channel in the 5.7 GHz band. They showed the feasibility of achieving 10 ms delivery delay. Khorov et al. [86] presented the periodic reservation methods available in various 802.11 standards including 802.11s, 802.11ad, 802.11ax, and 802.11be. They also addressed the challenges of establishing communication reservation periods for exchanging real-time multimedia traffic between two stations in the presence of interference. The use of 802.11 standards in real-time multimedia applications has been studied in [87] and [88]. Seno et al. [37] proposed a centrally-controlled 802.11 network to decide about the admission of nodes that require real-time communication. They proposed to use a Earliest Deadline First (EDF) scheduling method to admit nodes into the network subject to their deadline and retransmission requirements. To account for packet loss, the central controller uses an EDF strategy to schedule retransmissions. Their proposed method has been implemented on the Linux operating system and the ath9k driver.

Backscatter communication has been proposed to provide compatibility with the 802.11 standard while also supporting very low energy consumption. Mitsugi et al. [89] proposed a wireless and batteryless WSN for vibration testing of space structures. Their solution uses passive backscatter technology [90] that reflects energy from existing RF signals. The system consumes 300 μ A using a 4 MHz processor, supports 70 sensor nodes, its maximum sampling rate is 100 Hz, and data rate is 5 Mbps. The communication range is less than 5 m, which is not suitable for large structures.

XI. CONCLUSION

This paper presented Sensifi, a system based on the 802.11 (WiFi) standard for ultra-high-rate sensing applications. Our main observations and contributions are as follows: (i) We showed that timestamp encoding is necessary to reduce the overhead of data transmission. We proposed a lossless encoding method that achieves a high compression rate and low processing overhead. (ii) Considering the unique operational phases of the 802.11 standard, we proposed methods to enhance network longevity. In particular, we showed that periodic reassociation with the AP may be preferred over long beacon reception intervals. (iii) We profiled the overhead of various network stacks in terms of outgoing

packet preparation, processing, and their impact on sampling rate and stability. We significantly reduced packet processing overhead by bypassing the UDP layer. We also minimized the effect of packet processing on sampling stability by implementing a blocking packet processing call. (iv) We studied the delay of processing time synchronization packets from firmware to the application layer. We proved that firmware-based processing is necessary to achieve a sub- μ s accuracy. (v) We proposed a low-power node design for ultra-high-rate applications, and presented empirical micro-benchmarks and overall system evaluation results using this node design. Our work leveraged the two widely used RTOSs (FreeRTOS and ThreadX) and three low-power network stacks (NetX, NetXDuo, and LwIP).

Although the proposed system provides live sample transmission, no per-packet delivery delay is enforced. To enable the adoption of the proposed work in applications where real-time data delivery is a requirement [6], an area of future work is to establish a time-slotted channel access scheduling among nodes. Another area of future work is to evaluate the proposed system using a large number of nodes and considering various channel access methods. Novel methods must also be developed for systems that include more than one AP. For example, managing the association point of each node can be leveraged to reduce the number of retransmissions and enhance system reliability. Evaluating the proposed enhancements on various hardware platforms and using different 802.11 standards is left as future work.

ACKNOWLEDGMENT

The authors would like to thank engineers at Space Systems Loral (SSL) for their constructive feedback during this research.

REFERENCES

- [1] D. C. Betz, G. Thursby, B. Culshaw, and W. J. Staszewski, "Structural damage location with fiber bragg grating rosettes and lamb waves," *Structural health monitoring*, vol. 6, no. 4, pp. 299–308, 2007.
- [2] T. H. Loutas, A. Panopoulou, D. Roulias, and V. Kostopoulos, "Intelligent health monitoring of aerospace composite structures based on dynamic strain measurements," *Expert Systems with Applications*, vol. 39, no. 9, pp. 8412–8422, 2012.
- [3] J. K. Notay and G. A. Safdar, "A wireless sensor network based structural health monitoring system for an airplane," in *International Conference on Automation and Computing (ICAC)*. IEEE, 2011, pp. 240–245.
- [4] Q. Huang, B. Tang, and L. Deng, "Development of high synchronous acquisition accuracy wireless sensor network for machine vibration monitoring," *Measurement*, vol. 66, pp. 35–44, 2015.
- [5] L. Girard, S. Gruber, S. Weber, and J. Beutel, "Environmental controls of frost cracking revealed through in situ acoustic emission measurements in steep bedrock," *Geophysical Research Letters*, vol. 40, no. 9, pp. 1748–1753, 2013.
- [6] B. Dezfouli, M. Radi, and O. Chipara, "Rewimo: A real-time and reliable low-power wireless mobile network," *ACM Transactions on Sensor Networks (TOSN)*, vol. 13, no. 3, pp. 1–42, 2017.
- [7] S. Wijetunge, U. Gunawardana, and R. Liyanapathirana, "Wireless sensor networks for structural health monitoring: Considerations for communication protocol design," in *International Conference on Telecommunications (ICT)*. IEEE, 2010, pp. 694–699.

- [8] X. Liu, J. Cao, and P. Guo, "SenetSHM: Towards practical structural health monitoring using intelligent sensor networks," in *Big Data Cloud Comput. Soc. Comput. Netw. Sustain. Comput. Commun. (BDCloud-SocialCom-SustainCom)*. IEEE, 2016, pp. 416–423.
- [9] T. Harms, S. Sedigh, and F. Bastianini, "Structural health monitoring of bridges using wireless sensor networks," *IEEE Instrumentation and Measurement*, vol. 13, no. 6, pp. 14–18, 2010.
- [10] N. Xu, S. Rangwala, K. K. Chintalapudi, D. Ganesan, A. Broad, R. Govindan, and D. Estrin, "A wireless sensor network for structural monitoring," in *International Conference on Embedded Networked Sensor Systems (SenSys)*, 2004, pp. 13–24.
- [11] National Aeronautics and Space Administration. (2015) Vibration Testing. [Online]. Available: https://www.nasa.gov/centers/johnson/pdf/639713main_Vibration_Testing_FTI.pdf
- [12] P. M. Fantasia. (2011) Vibration and Acoustic Test Facility (VATF): User Test Planning Guide. [Online]. Available: https://www.nasa.gov/centers/johnson/pdf/639503main_VATF_User_Test_Planning_Guide.pdf
- [13] M. Lindstrom. (2019) What's wrong with my piezoelectric accelerometer? [Online]. Available: http://www.pcb.com/Contentstore/MktgContent/LinkedDocuments/Technotes/TN-30-what's_wrong_Lowres.pdf
- [14] M. Luvisotto, Z. Pang, and D. Dzung, "Ultra high performance wireless control for critical applications: Challenges and directions," *IEEE Transactions on Industrial Informatics*, vol. 13, no. 3, pp. 1448–1459, 2017.
- [15] B. Dezfouli, M. Radi, S. Abd Razak, T. Hwee-Pink, and K. A. Bakar, "Modeling low-power wireless communications," *Journal of Network and Computer Applications*, vol. 51, pp. 102–126, 2015.
- [16] Microsoft Inc. (2020) HART Communication Protocol Specification, Revision 7.7. [Online]. Available: <https://library.fieldcommgroup.org/20013/TS20013/7.7/#page=1>
- [17] IEC. (2015) Industrial networks - Wireless communication network and communication profiles - WIA-PA. [Online]. Available: <https://webstore.iec.ch/publication/23902>
- [18] ISA 100 Wireless. (2020) ISA 100 Wireless. [Online]. Available: <https://isa100wci.org>
- [19] R. Heynricke, D. Krush, G. Scholl, B. Kaercher, J. Ritter, P. Gaggero, and M. Rentschler, "IO-link wireless enhanced sensors and actuators for industry 4.0 networks," in *AMA Conferences*, 2017, pp. 134–138.
- [20] G. Scheible, D. Dzung, J. Endresen, and J. E. Frey, "Unplugged but connected [design and implementation of a truly wireless real-time sensor/actuator interface]," *IEEE Industrial Electronics Magazine*, vol. 1, no. 2, pp. 25–34, 2007.
- [21] S. Valenti, M. Conti, P. Pierleoni, L. Zappelli, A. Belli, F. Gara, S. Carbonari, and M. Regni, "A low cost wireless sensor node for building monitoring," in *Workshop on Environmental, Energy, and Structural Monitoring Systems (EESMS)*. IEEE, 2018, pp. 1–6.
- [22] S. Kim, S. Pakzad, D. Culler, J. Demmel, G. Fenves, S. Glaser, and M. Turon, "Health monitoring of civil infrastructures using wireless sensor networks," in *International Conference on Information Processing in Sensor Networks (IPSN)*, 2007, pp. 254–263.
- [23] A. Araujo, J. García-Palacios, J. Blesa, F. Tirado, E. Romero, A. Samartín, and O. Nieto-Taladriz, "Wireless measurement system for structural health monitoring with high time-synchronization accuracy," *IEEE Transactions on Instrumentation and Measurement*, vol. 61, no. 3, pp. 801–810, 2011.
- [24] A. Woo, T. Tong, and D. Culler, "Taming the underlying challenges of reliable multihop routing in sensor networks," in *International Conference on Embedded Networked Sensor Systems (SenSys)*, 2003, pp. 14–27.
- [25] K. Chintalapudi, T. Fu, J. Paek, N. Kothari, S. Rangwala, J. Caffrey, R. Govindan, E. Johnson, and S. Masri, "Monitoring civil structures with a wireless sensor network," *IEEE Internet Computing*, vol. 10, no. 2, pp. 26–34, 2006.
- [26] X. Liu, J. Cao, S. Lai, C. Yang, H. Wu, and Y. L. Xu, "Energy efficient clustering for wsn-based structural health monitoring," in *International Conference on Computer Communications (INFOCOM)*. IEEE, 2011, pp. 2768–2776.
- [27] Q. Hu, X. Liu, Q. Wu, J. Cao, Y. Liu, and Y. Tan, "Cluster-based energy-efficient structural health monitoring using wireless sensor networks," in *International Conference on Computer Science and Service System (CSSS)*. IEEE, 2012, pp. 1951–1956.
- [28] Q. Ling, Z. Tian, Y. Yin, and Y. Li, "Localized structural health monitoring using energy-efficient wireless sensor networks," *IEEE Sensors Journal*, vol. 9, no. 11, pp. 1596–1604, 2009.
- [29] G. Werner-Allen, K. Lorincz, M. Ruiz, O. Marcillo, J. Johnson, J. Lees, and M. Welsh, "Deploying a wireless sensor network on an active volcano," *IEEE Internet Computing*, vol. 10, no. 2, pp. 18–25, 2006.
- [30] M. J. Whelan, M. V. Gangone, K. D. Janoyan, and R. Jha, "Real-time wireless vibration monitoring for operational modal analysis of an integral abutment highway bridge," *Engineering Structures*, vol. 31, no. 10, pp. 2224–2235, 2009.
- [31] E. Sazonov, V. Krishnamurthy, and R. Schilling, "Wireless intelligent sensor and actuator network—a scalable platform for time-synchronous applications of structural health monitoring," *Structural Health Monitoring*, vol. 9, no. 5, pp. 465–476, 2010.
- [32] D. Phanish, P. Garver, G. Matalkah, T. Landes, F. Shen, J. Dumond, R. Abler, D. Zhu, X. Dong, Y. Wang *et al.*, "A wireless sensor network for monitoring the structural health of a football stadium," in *World Forum on Internet of Things (WF-IoT)*. IEEE, 2015, pp. 471–477.
- [33] G. Yan and S. J. Dyke, "Structural damage detection robust against time synchronization errors," *Smart Materials and Structures*, vol. 19, no. 6, p. 065001, 2010.
- [34] B. Dezfouli, M. Radi, and O. Chipara, "Mobility-aware real-time scheduling for low-power wireless networks," in *International Conference on Computer Communications (INFOCOM)*. IEEE, 2016, pp. 1–9.
- [35] M. M. Alves, L. Pirmez, S. Rossetto, F. C. Delicato, C. M. de Farias, P. F. Pires, I. L. dos Santos, and A. Y. Zomaya, "Damage prediction for wind turbines using wireless sensor and actuator networks," *Journal of Network and Computer Applications*, vol. 80, pp. 123–140, 2017.
- [36] Y.-H. Wei, Q. Leng, S. Han, A. K. Mok, W. Zhang, and M. Tomizuka, "RT-WiFi: Real-time high-speed communication protocol for wireless cyber-physical control applications," in *Real-Time Systems Symposium (RTSS)*, 2013, pp. 140–149.
- [37] L. Seno, G. Cena, S. Scanzio, A. Valenzano, and C. Zunino, "Enhancing communication determinism in Wi-Fi networks for soft real-time industrial applications," *IEEE Transactions on Industrial Informatics*, vol. 13, no. 2, pp. 866–876, 2016.
- [38] M. Islam, N. N. Soualihu, and S. Faizullah, "Structural health monitoring by payload compression in wireless sensors network: An algorithmic analysis," *International Journal of Engineering and Management Research (IJEMR)*, vol. 8, no. 3, pp. 184–190, 2018.
- [39] Amazon Inc. (2020) FreeRTOS: Real-time operating system for microcontrollers. [Online]. Available: <https://www.freertos.org>
- [40] Amazon Inc. (2020) FreeRTOS AWS Reference Integrations. [Online]. Available: <https://github.com/aws/amazon-freertos>
- [41] Microsoft Inc. (2020) Azure RTOS ThreadX documentation. [Online]. Available: <https://docs.microsoft.com/en-us/azure/rtos/threadx/>
- [42] Microsoft Inc. (2020) Azure RTOS ThreadX. [Online]. Available: <https://github.com/azure-rtos/threadx>
- [43] Free Software Foundation Inc. (2020) LwIP: A Lightweight TCP/IP stack. [Online]. Available: <https://savannah.nongnu.org/projects/lwip/>
- [44] Microsoft Inc. (2020) Azure RTOS NetX documentation. [Online]. Available: <https://docs.microsoft.com/en-us/azure/rtos/netx/>
- [45] Microsoft Inc. (2020) Azure RTOS NetX Duo documentation. [Online]. Available: <https://docs.microsoft.com/en-us/azure/rtos/netx-duo/>
- [46] K. Chang, "Deep space 1 spacecraft vibration qualification testing," *Institute of Environmental Sciences and Technology 46th Annual Technical Meeting*, 2000.
- [47] A. R. Kolaini, W. Tsuha, and J. P. Fernandez, "Spacecraft vibration testing: Benefits and potential issues," *Advances in Aircraft and Spacecraft Science*, vol. 5, no. 2, p. 165, 2018.
- [48] S. Gordon and D. L. Kern, "Benefits of spacecraft level vibration testing," *Aerospace Testing Seminar (ATS)*, 2015.
- [49] D. L. Kern, S. A. Gordon, and T. D. Scharton, "Nasa handbook for spacecraft structural dynamics testing," in *Spacecraft Structures, Materials and Mechanical Testing*, vol. 581, 2005.
- [50] J. Dodson and A. Eglin, "High-g Shocking Testing of the Martlet Wireless Sensing System," *Sound & Vibration*, p. 6, 2018.

- [51] M. D. Kaffle, D.-O. Lee, J. Lee, J.-H. Han, S.-H. Woo *et al.*, "Numerical modeling of shock generation and propagation during satellite separation," in *The World Congress on Advances in Structural Engineering and Mechanics*, 2013, pp. 1868–1885.
- [52] Cypress Semiconductor Corporation. (2020) CYW54907 - WICED™ IEEE 802.11 a/b/g/n/ac SoC with an Embedded Applications Processor. [Online]. Available: <https://www.cypress.com/file/407801/download>
- [53] G. R. Mendez, M. A. M. Yunus, and S. C. Mukhopadhyay, "A WiFi based smart wireless sensor network for monitoring an agricultural environment," in *International Instrumentation and Measurement Technology Conference (I2MTC)*. IEEE, 2012, pp. 2640–2645.
- [54] Y. Zhai, J. Li, C. Ding, S. Luan, and M. Jin, "A Sample-and-Hold Circuit for a Resolution Pipelined ADC," in *International Conference on Energy, Environment and Sustainable Development (ICEESD)*. Atlantis Press, 2018.
- [55] T. E. Becker, A. J. Lanot, G. S. Cardoso, and T. R. Balen, "Single event transient effects on charge redistribution SAR ADCs," *Microelectronics Reliability*, vol. 73, pp. 22–35, 2017.
- [56] W. Kester, "ADC architectures II: successive approximation ADCs," *MT-021 Tutorial, Analog Devices*, 2009.
- [57] T. H. Cormen, C. E. Leiserson, R. L. Rivest, and C. Stein, *Introduction to algorithms*. MIT press, 2009.
- [58] D. E. Knuth, *The art of computer programming: Volume 3: Sorting and Searching*. Addison-Wesley Professional, 1998.
- [59] F. Tirado-Andrés and A. Araujo, "Performance of clock sources and their influence on time synchronization in wireless sensor networks," *International Journal of Distributed Sensor Networks*, vol. 15, no. 9, p. 1550147719879372, 2019.
- [60] Cypress Semiconductor Corporation. (2020) CYW43907 - WICED™ IEEE 802.11 a/b/g/n SoC with an Embedded Applications Processor. [Online]. Available: <https://www.cypress.com/file/298236/download>
- [61] A. Abedi, O. Abari, and T. Brecht, "Wi-le: Can wifi replace bluetooth?" in *Proceedings of the 18th ACM Workshop on Hot Topics in Networks*, 2019, pp. 117–124.
- [62] Analog Devices Inc. (2018) ADXL1004 MEMS Accelerometer. [Online]. Available: <https://www.analog.com/media/en/technical-documentation/data-sheets/adx11004.pdf>
- [63] Analog Devices Inc. (2017) AD4000/AD4004/AD4008 16-Bit, 2 M/1 M/500 ksp/s, Precision, Pseudo Differential, SAR ADCs. [Online]. Available: <https://www.analog.com/media/en/technical-documentation/data-sheets/AD4000-4004-4008.pdf>
- [64] Linear Technology. (2010) LTC2941-1 1 A I²C Battery Gas Gauge. [Online]. Available: <https://www.analog.com/media/en/technical-documentation/data-sheets/29411f.pdf>
- [65] Texas Instruments. (2019) TPS6302x buck-boost converter. [Online]. Available: <http://www.ti.com/lit/ds/symlink/tps63020.pdf>
- [66] Texas Instruments. (2015) TPS737xx 1 A Low-Dropout Regulator. [Online]. Available: <http://www.ti.com/lit/ds/symlink/tps737.pdf>
- [67] Texas Instruments. (2015) TPS780xx 150 mA Low-Dropout Regulator. [Online]. Available: <http://www.ti.com/lit/ds/symlink/tps780.pdf>
- [68] Linear Technology. (1999) LT1461 Voltage Reference. [Online]. Available: <https://www.analog.com/media/en/technical-documentation/data-sheets/1461fb.pdf>
- [69] Texas Instruments. (2015) INA219 Current/Power Monitor. [Online]. Available: <http://www.ti.com/lit/ds/symlink/ina219.pdf>
- [70] Texas Instruments. (2018) Tips and tricks for designing with voltage references. [Online]. Available: <http://www.ti.com/lit/ml/slyc147/slyc147.pdf>
- [71] B. Dezfouli, I. Amirtharaj, and C.-C. C. Li, "Empiot: An energy measurement platform for wireless iot devices," *Journal of Network and Computer Applications*, vol. 121, pp. 135–148, 2018.
- [72] Tektronix, Inc. (2017) DMM7510 7½-Digit Graphical Sampling Multimeter. [Online]. Available: <https://www.tek.com/tektronix-and-keithley-digital-multimeter/dmm7510>
- [73] J. M. Samuels, M. Reyer, S. Hurlebaus, S. H. Lucy, D. G. Woodcock, and J. M. Bracci, "Wireless sensor network to monitor an historic structure under rehabilitation," *Journal of Civil Structural Health Monitoring*, vol. 1, no. 3–4, pp. 69–78, 2011.
- [74] J. P. Lynch, K. H. Law, A. S. Kiremidjian, E. Carryer, C. R. Farrar, H. Sohn, D. W. Allen, B. Nadler, and J. R. Wait, "Design and performance validation of a wireless sensing unit for structural monitoring applications," *Structural Engineering and Mechanics*, vol. 17, no. 3–4, pp. 393–408, 2004.
- [75] B. Bengerherbia, M. O. Zmirli, A. Toubal, and A. Guessoum, "FPGA-based wireless sensor nodes for vibration monitoring system and fault diagnosis," *Measurement*, vol. 101, pp. 81–92, 2017.
- [76] L. Swathy and L. Abraham, "Analysis of vibration and acoustic sensors for machine health monitoring and its wireless implementation for low cost space applications," in *International Conference on Computational Systems and Communications (ICCSC)*. IEEE, 2014, pp. 80–85.
- [77] S. Weber, S. Gruber, L. Girard, J. Beutel, and K. M. Hinkel, "Design of a measurement assembly to study in situ rock damage driven by freezings," in *International Conference on Permafrost (ICOP)*. University of Zurich, 2012, pp. 437–442.
- [78] B. Dezfouli, M. Radi, K. Whitehouse, S. A. Razak, and H.-P. Tan, "Cama: Efficient modeling of the capture effect for low-power wireless networks," *ACM Transactions on Sensor Networks (TOSN)*, vol. 11, no. 1, pp. 1–43, 2014.
- [79] K. Mechitov, W. Kim, G. Agha, and T. Nagayama, "High-frequency distributed sensing for structure monitoring," in *Proc. First Intl. Workshop on Networked Sensing Systems (INSS 04)*, 2004, pp. 101–105.
- [80] A. Girolami, D. Brunelli, and L. Benini, "Low-cost and distributed health monitoring system for critical buildings," in *Workshop on Environmental, Energy, and Structural Monitoring Systems (EESMS)*. IEEE, 2017, pp. 1–6.
- [81] X. Dai, S. Gao, K. Pan, J. Zhu, and H. F. Rashvand, "Wireless piezoelectric sensor systems for defect detection and localization," in *Wireless Sensor Systems for Extreme Environments: Space, Underwater, Underground and Industrial*. John Wiley & Sons, 2017, pp. 201–219.
- [82] F. Tamarin, S. Vitturi, M. Luvisotto, and A. Zanella, "On the use of IEEE 802.11n for industrial communications," *IEEE Transactions on Industrial Informatics*, vol. 12, no. 5, pp. 1877–1886, 2015.
- [83] Y. Yu, F. Han, Y. Bao, and J. Ou, "A study on data loss compensation of wifi-based wireless sensor networks for structural health monitoring," *IEEE Sensors Journal*, vol. 16, no. 10, pp. 3811–3818, 2015.
- [84] P. Bartolomeu, M. Alam, J. Ferreira, and J. A. Fonseca, "Supporting deterministic wireless communications in industrial IoT," *IEEE Transactions on Industrial Informatics*, vol. 14, no. 9, pp. 4045–4054, 2018.
- [85] C. Dombrowski and J. Gross, "EchoRing: A low-latency, reliable token-passing MAC protocol for wireless industrial networks," in *Proceedings of European Wireless Conference*. VDE, 2015, pp. 1–8.
- [86] E. Khorov, A. Lyakhov, A. Ivanov, and I. F. Akyildiz, "Modeling of Real-Time Multimedia Streaming in Wi-Fi Networks With Periodic Reservations," *IEEE Access*, vol. 8, pp. 55 633–55 653, 2020.
- [87] J. S. Blanes, J. Berenguer-Sebastiá, V. Sempere-Paya, and D. T. Ferrandis, "802.11n performance analysis for a real multimedia industrial application," *Computers in Industry*, vol. 66, pp. 31–40, 2015.
- [88] S. Santonja-Climent, D. Todoli-Ferrandis, T. Albero-Albero, V.-M. Sempere-Payá, J. Silvestre-Blanes, and J. Alcobér, "Analysis of control and multimedia real-time traffic over SIP and RTP on 802.11n wireless links for utilities networks," in *Conference on Emerging Technologies & Factory Automation (ETFA)*. IEEE, 2010, pp. 1–4.
- [89] J. Mitsugi, N. Rajoria, Y. Kawakita, and H. Ichikawa, "Wireless and batteryless vibration testing of space structures with implanted lsi sensors," in *International Astronautical Congress (IAC)*, 2017.
- [90] D. Bharadia, K. R. Joshi, M. Kotaru, and S. Katti, "Backfi: High throughput wifi backscatter," *ACM SIGCOMM Computer Communication Review*, vol. 45, no. 4, pp. 283–296, 2015.